Title: Analysis of the effect of formulation properties and process parameters on granule formation in twin-screw wet granulation.

Authors: Michiel Peeters, Ana Alejandra Barrera Jimenez, Kensaku Matsunami, Michael Ghijs, Eduardo Dos Santos Schultz, Mina Roudgar, Tamas Vigh, Fanny Stauffer, Ingmar Nopens, Thomas De Beer

Abstract

In the last few years, twin-screw wet granulation (TSWG) has become one of the key continuous pharmaceutical unit operations. Despite the many studies that have been performed, only little is known about the effect of the starting material properties on the stepwise granule formation along the length of the twin-screw granulator (TSG) barrel. Hence, this study obtained a detailed understanding of the effect of formulation properties (i.e., Active Pharmaceutical Ingredient (API) properties, formulation blend particle size distribution and formulation drug load) and process settings on granule formation in TSWG. An experimental set-up was used allowing the collection of granules at the different TSG compartments. Granules were characterized in terms of granule size, shape, binder liquid and API distributions. Liquid-to-solid (L/S) ratio was the only TSG process parameter impacting the granule size and shape evolution. Particle size and flow properties (e.g., flow rate index) had an important effect on the granule size and shape changes whereas water-related properties (e.g., water binding capacity and solubility) became influential at the last TSG compartments. The API solubility and L/S ratio were found to have a major impact on the distribution of binder liquid over the different granule size fractions. In the first TSG compartment (i.e., wetting compartment), the distribution of the API in the granules was influenced by its solubility in the granulation liquid.

1. Introduction

Over the last years, continuous manufacturing has gained momentum in the pharmaceutical industry due to its several advantages compared to batch manufacturing. One of the main advantages of continuous manufacturing is its flexibility with respect to batch size, which can be adjusted by simply changing the total operating time. Therefore, time-consuming process scale-up studies can be avoided (Lee et al., 2015). Secondly, continuous processes are ideally suited for real-time monitoring and control of the product quality by the implementation of Process Analytical Technology (PAT)-tools (Fonteyne et al., 2015). Among the different continuous manufacturing routes, direct compression is the most simple and cost-effective option. However, direct compression is not suitable for active pharmaceutical ingredients (APIs) with poor flow properties or insufficient compactibility. Twin-screw wet granulation (TSWG) is the most studied continuous granulation technology (Vervaet and Remon, 2005) as an intermediate manufacturing operation for those materials.

In order to develop robust TSWG processes, the U.S. Food and Drug Administration (FDA) encourages the use of an enhanced development approach, i.e., quality by design (QbD) (FDA, 2004). The essence of the QbD principle is that quality ought to be built in the manufacturing process or, in other words, that processes are well understood to consistently ensure a predefined quality of the end product. In the QbD framework, mathematical models can be used at every stage of product development and manufacturing to enhance process and product understanding as well as to predict quality properties (Kourti et al., 2014). Mathematical models may be first-principles, mechanistic models, phenomenological, data-driven or hybrid models. Mechanistic models make hypotheses on the mechanisms occurring in the system and thus their application for TSWG requires a detailed understanding of the

underlying granulation physics occurring within the different compartments of the twin-screw granulator (TSG) unit (Kumar et al., 2013).

Many different studies have been performed to better understand the granule formation mechanisms in TSWG. A number of researchers evaluated the effect of the screw elements and their specifications on granule formation. Dhenge et al. (2012) studied the change of granules in terms of size, shape and strength along the length of the screws in a TSG. Granules were found to become more spherical and stronger towards the TSG outlet. The kneading elements promoted consolidation and breakage while the conveying elements led to coalescence, breakage and some consolidation. Li et al. (2019) evaluated the effect of conveying elements, kneading elements and distributive mixing elements on granule size, porosity, and binder liquid concentration uniformity in a TSG. The conveying elements did not significantly modify the granule properties whereas the granule size increased, porosity decreased, and binder liquid concentration uniformity increased downstream of the kneading or distributive mixing elements. Liu et al. (2015) studied the effect of the pitch length of conveying elements on final granule particle size, shape, porosity and fracture strength. A higher conveying element pitch length increased the granule size and aspect ratio (i.e., sphericity) of the granules at the TSG outlet by increasing the particle velocity. Mundozah et al. (2019a) focused on the effect of screw element type on the reduction of fines (<150 µm) for different formulations with varying hydrophilicity (i.e., by changing the amount lactose and magnesium stearate in the formulation). The different screw elements used were conveying elements (CE), kneading elements (KE) and tooth mixing elements (TME). The order of reduction in the amount of fines was observed to be CE < KE < TME, particularly with increase in formulation hydrophobicity. This was probably due to the progressively improved liquid distribution with increase in material residence time, which resulted in the greater extent of granule formation and less production of fines.

Several researchers studied the impact of process settings on granule formation mechanisms. Verstraeten et al. (2017) analyzed the effect of different TSG process settings such as liquid-to-solid (L/S) ratio, mass feed rate (MFR) and screw speed (SS) upon granule formation using both a hydrophilic and hydrophobic formulation. Granule characteristic data-collection such as size, shape, liquid and porosity distribution were measured at the different compartments along the length of the granulator barrel by changing the location of liquid addition or screw configurations. The experimental results indicated that L/S ratio was the most important process parameter dictating the formation of the granules and their corresponding properties, by regulating the degree of aggregation and breakage in the different compartments along the internal length of the twin-screw granulator barrel. The granule property data that was collected in this study and the obtained knowledge were later used to construct a compartmental Population Balance Model (PBM) simulating the granule size distribution both inside the intermediate TSG compartments as well as at the outlet of the TSG (Van Hauwermeiren et al., 2018).

In most of the aforementioned studies, only one specific formulation or a few formulations containing no API (i.e., placebo formulations) were used. Thus, the effect of API properties on granule formation along the length of the TSG barrel is currently missing. The PBM that was presented by Van Hauwermeiren et al. (2018) was developed using data for one specific formulation and hence cannot be used to predict the granule size distribution based on the starting material properties of a new API. While this PBM was extended to a two-dimensional model that can compute granule size and porosity (Barrera Jiménez et al., 2023a), the impact of API properties were not analyzed. In order to improve the usability of such PBMs in TSWG process and formulation development, the impact of API properties on the granule formation mechanisms needs to be understood.

The goal of this study was to understand the effect of formulation properties (i.e., API properties, formulation blend particle size distribution and formulation drug load) and process settings on granule formation in TSWG. Accordingly, granule properties such as size, shape, binder liquid and API distribution were determined at four intermediate TSG compartments for formulations with a fixed excipient base and containing APIs with different physicochemical properties. The properties of the granules were compared between formulations containing a low and high concentration of API. Furthermore, these formulations were manufactured under different process settings such as L/S ratio, MFR and SS to evaluate the impact of process settings on granule formation. The detailed understanding of the effect of raw material properties and process parameters on the granulation process can be used as a key input for the development of generic mechanistic models that can simulate granule quality attributes of a new formulation (e.g., Barrera Jiménez et al., 2023b).

2. Materials

The raw materials and formulations that were used and the details of the granulation experiments were already described in two previous publications from our research group (Peeters et al., 2023a, 2023b). Only the parts relevant for this work are given in the main manuscript, and the reader can find more details in the appendix or the previous publications.

α-Lactose (Pharmatose 200M) (DFE Pharma, Veghel, The Netherlands) and microcrystalline cellulose (MCC) (Avicel PH 101, FMC Biopolymer, Cork, Ireland) were used as fillers (Table 1). Hydroxypropylmethylcellulose (HPMC) (Methocel E15 LV, Dow Chemical Company, Midland, MI, USA) was used as a dry binder. Ten active pharmaceutical ingredients (APIs) with large differences in physicochemical properties (e.g., hydrophilicity and flow properties), were used (Table 1). In this study, the same chemical compounds with different grades were defined as different materials. The raw materials were extensively characterized in a previous study (Peeters et al., 2023a). Some APIs were obtained via Janssen Pharmaceutica (Geel, Belgium), the other APIs were purchased from UTAG (Almere, The Netherlands), Mallinckrodt Pharmaceuticals (Dublin, Ireland), and BASF (Ludwigshafen, Germany), and the API suppliers are given in Table 1.

Table 1 Overview of the used raw materials.

Material	Type	Grade	Solubility[1]	Supplier	Abbreviation
Hydrochlorothiazide	API	Regular	Very slightly soluble	UTAG	HCT
API 2 Regular	API	Regular	Freely soluble	Janssen	2_r
API 2 Fine	API	Fine	Freely soluble	Janssen	2_f
API 3 Fine	API	Fine	Freely soluble	UCB	3_f
API 4 Regular	API	Regular	Practically insoluble	Janssen	4_r
API 4 fine	API	Fine	Practically insoluble	Janssen	4_f
Paracetamol	API	Semi-Fine	Sparingly soluble	Mallinckrodt Pharmaceuticals	P_sf
Paracetamol	API	Dense	Sparingly soluble	Mallinckrodt Pharmaceuticals	P_d
Theophylline, anhydrous	API	200M	Slightly soluble	BASF	T_A_200
Ibuprofen	API	50	Practically insoluble	BASF	Ibu
α-lactose (Pharmatose)	Filler	200M	NA	DFE Pharma	200M
Microcrystalline cellulose (MCC) (Avicel)	Filler	PH101	NA	FMC BioPolymer	PH101
Hydroxypropylmethylcellulose (HPMC) (Methocel)	Binder	E15 LV	NA	Dow Chemical Company	E15

[1]solubility of the active pharmaceutical ingredients (APIs) according to the classification of the USP

3. Methods

The experimental work described in this paper is an extension of the research of Peeters et al. (2023a,b), and only a summary of the parts relevant to the research question and scope of this paper is given. For a more detailed description of the experimental analysis, the reader is referred to the appendix or the aforementioned work.

3.1 Formulation and API variation

The APIs from Table 1 were combined with a fixed excipient base into 13 different formulations having a drug load of 5 % w/w or 50 % w/w (Table 2). The excipient base consisted of 15 % w/w Avicel PH101, 5 % w/w Methocel E15 LV, and 30 % w/w or 75 % w/w Pharmatose 200M for the high and low drug load formulations, respectively. As the composition of the excipient base was fixed, the effect of API physicochemical properties on granulation could be studied directly.

Table 2. Overview of the used formulations.

Formulation	API name	API grade	Abbreviation	API concentration (% w/w)	Factors[1]	L/S ratio (%)[2]
H5	Hydrochlorothiazide	Regular	HCT	5	MFR, LS	8.9 – 20.2
H50	Hydrochlorothiazide	Regular	HCT	50	MFR, LS	15.1 – 23.7
2R5	API 2	Regular	2_r	5	MFR, SS, LS	8.0 – 18.0
2R50	API 2	Regular	2_r	50	MFR, SS, LS	5.2 – 16.0
2F50	API 2	Fine	2_f	50	MFR, SS, LS	5.2 – 16.0
3F5	API 3	Fine	3_f	5	MFR, SS, LS	8.0 – 16.0
3F50	API 3	Fine	3_f	50	MFR, SS, LS	7.2 – 10.0
4R50	API 4	Regular	4_r	50	MFR, SS, LS	20.0 – 28.0
4F50	API 4	Fine	4_f	50	MFR, SS, LS	20.0 – 28.0
PD50	Paracetamol	Dense	P_d	50	MFR, SS, LS	15.9 – 25.2
PSF50	Paracetamol	Semi-fine	P_sf	50	MFR, SS, LS	13.0 – 25.2
I50	Ibuprofen	50	Ibu	50	MFR, SS, LS	18.0 – 28.0
T50	Theophylline, anhydrous	200M	T_A_200	50	LS	15.0 – 23.5

[1]The process parameters (factors) that were varied for each formulation during the granulation experiments were mass feed rate (MFR), screw speed (SS) and liquid-to-solid ratio (LS)
[2]lowest and highest L/S ratio applied for each formulation

3.2 Raw material characterization

The powders (Table 1) were characterized to obtain a raw material property database consisting of 44 physicochemical properties of the APIs, fillers and binder (Table 3). The formulation blends (Table 2) were characterized using laser diffraction to obtain 7 particle size descriptors (Table 3). Detailed characterization methods can be seen in the appendix or Peeters et al. (2023b).

Table 3. Overview of the characterization techniques with their corresponding properties (descriptors) and utilized abbreviations.

Characterization technique	Descriptor	Abbreviation
Laser diffraction using wet dispersion[1]	10, 50 and 90% cumulative undersize of volumetric PSD	d0.1, d0.1_F, d0.5, d0.5_F, d0.9, d0.9_F
	Volume and surface-weighted mean particle size	D[4,3], D[4,3]_F, D[3,2], D[3,2]_F
	Width and span of volumetric PSD	dWidth, dWidth_F, span, span_F
Powder density and porosity	Bulk and tapped density	ρb, ρt
	Compressibility index and hausner ratio	CI, HR
	True density and porosity	ρtrue, ε
Water binding capacity	Water binding capacity	WBC
Contact angle	Contact angle after 1, 30 and 60 s	CA1, CA30, CA60

Solubility[2]	Maximum solubility in water	S_{max}
Loss on drying	Moisture content	LoD
Angle of repose	Angle of repose and cohesion	AoR, SCI
Dissolution rate[2]	Fraction powder dissolved after 1', 3', 5', 10', 20', 30' and 60'	DR1, DR3, DR5, DR10, DR20, DR30, DR60
Specific surface area	Specific surface area	SSA
Ring shear test	Flow function coefficient, unconfined yield stress, major principal stress	ffc, σ_c, σ_1
	Bulk density-weighted flow	ff_{rho}
	linear angle of internal friction, effective angle of internal friction, angle of internal friction at steady state flow	φ_{lin}, φ_e, φ_{sf}
	cohesion	τ_c
	Bulk density	RHOB
Powder rheology: stability and variable flow rate	Basic flow energy, stability index, flow rate index, specific energy	BFE, SI, FRI, SE, CBD
Powder rheology: compressibility	Compressibility at 15 kPa	Cmpr

[1]also measured for formulation blends (F). [2]not measured for microcrystalline cellulose and hydroxypropylmethylcellulose.

3.3 Preparation and collection of granules

Before blending, all APIs were passed through a Quadro U5 Comil (1000 rpm, round holed screen, screen size 1397 µm, Quadro, Waterloo, Canada) to eliminate possible large agglomerates. Subsequently, for each blend formulation all the solid raw materials were mixed in a tumbling blender (Inversina Bioengineering, Wald, Switzerland) during 15 min at 25 rpm. Granules were then produced using the granulation module of the ConsiGma™-25 unit (GEA Pharma Systems, Wommelgem, Belgium). This granulation module consists of two 25 mm diameter co-rotating screws with a length-to-diameter (L/D) ratio of 20:1. The blend was fed gravimetrically to the granulation module using a K-tron KT20 loss-in-weight feeder (Coperion K-tron, Niederlenz, Switzerland). Binder liquid (i.e., demineralized water) was added before the first kneading zone (i.e., wetting compartment) by a twin-peristaltic pump. The pump was positioned out-of-phase and connected to silicon tubing with an internal diameter of 1.6 or 2.4 mm. The silicon tubes were connected to nozzles with an orifice of 0.8 or 1.6 mm. The selection of nozzles and tubes depended on the liquid flow rate.

After wetting, the wetted agglomerates were kneaded in a first kneading zone, consisting of 6 kneading elements with a L/D of 0.25 arranged at an angle of 60°. Granules were passing through another kneading zone arranged identically to the first kneading zone, by passing a small conveying zone of L = 1.5D. The granules were then transported by a conveying zone (L = 1.5D) towards the end of the granulator. At the end of the screws, three size control elements (SCE) (L = 1D for each size control element) were positioned to reduce the fraction of oversized granules. Before sampling, a stabilisation period was needed to reach steady-state conditions. All collected granules were tray-dried at room temperature (i.e., 25 °C) for 12 hours. Subsequently, the granules were oven dried (40°C, 25% RH) until a moisture content between 1 and 3% was obtained prior to further granule characterization. The moisture content was measured by drying 1 g of material at 105 °C until a stable mass was recorded over a period of 30 s (Mettler Toledo HC103 Halogen Moisture Analyzer, Mettler-Toledo, Zaventem, Belgium).

In order to experimentally characterize the change in granule properties (i.e., size, shape, binder liquid and API distribution) along the length of the granulator barrel, granule samples were collected in well-defined compartments of the TSG (Fig. 1). This method was described in detail in previous publications from our research group (Verstraeten et al., 2017; Peeters et al., 2023b).

Granule samples were collected in the following compartments:

- Compartment 1 (C1): Before the first kneading compartment, where the binder liquid is added (i.e., wetting compartment);
- Compartment 3 (C3): After the first kneading zone (KZ1);
- Compartment 5 (C5): After the second kneading zone (KZ2);
- Compartment 6 (C6): After the size control elements (SCE) (i.e., granulator outlet).

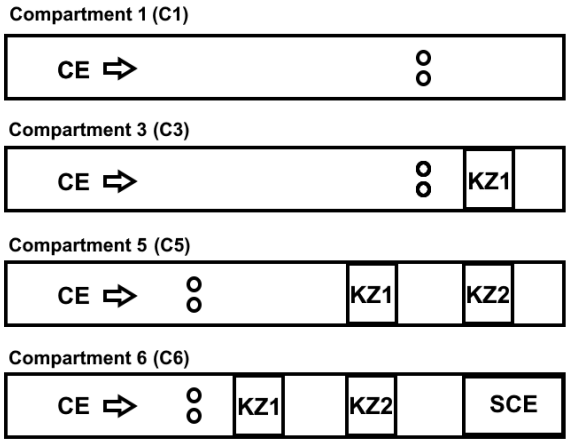

Fig. 1. Experimental set-up of the twin-screw wet granulation experiments. The direction of the powder flow is indicated by the arrow. Screw elements: conveying elements (CE), first kneading zone (KZ1), second kneading zone (KZ2) and size control elements (SCE). The liquid addition port is represented by the circles.

The first and second kneading zone (i.e., KZ1 and KZ2) represent compartments 2 (C2) and 4 (C4), respectively. By using a second liquid addition port and a screw configuration consisting of only conveying elements, granules collected at the TSG outlet reflect granules in the C1. By placing a kneading zone after the second liquid addition port, granules collected at the TSG outlet represent granules in C3. Samples at C5 can be collected at the TSG outlet by using the first liquid addition port and by leaving out the SCE at the end of the screw configuration.

This method allows to collect large amounts of granules at intermediate TSG compartments (i.e., C1, C3, C5) without the need for a screw pull-out, where only a limited amount of granules (±5 g) can be collected during each experiment (Li et al., 2014).

3.4 Experimental design

To investigate the influence of the granulation process parameters SS, MFR and L/S ratio on the granule size and shape distribution, per formulation, a central composite circumscribed Design of Experiments (CCC DoE) with two or three factors was performed (Table 2). The CCC DoEs were performed at four distinct TSG compartments (see Section 3.3). During preliminary experiments collecting granules at the granulator outlet (i.e., C6), SS was found to have a much smaller effect on granule size and shape compared to MFR and L/S for formulations H5 and H50 and hence SS was excluded as a factor from the DoE for these formulations. Each DoE resulted in 8 and 14 experiments when using two and three factors, respectively (see Table 2 for the number of factors applied to each formulation). Three centerpoint experiments were performed in each DoE. MFR and SS were varied from 15 to 25 kg/h and from 450 to 900 rpm, while the applicable L/S ratio ranges were experimentally determined for each formulation blend (Table 2). The applicable L/S ratio ranges were determined based on the method proposed by Peeters et al. (2023a). The minimum workable L/S ratio was established as the ratio at which small granules, with a diameter of approximately 220 µm (d10) and around 2200 µm (d90), were achieved. The maximum viable L/S ratio was

determined as the highest attainable ratio without inducing paste formation or overloading the granulator due to barrel obstruction. In total, the DoEs for all the formulations resulted in 768 experiments (i.e., 680 and 88 experiments for the 3 and 2 factor CCC DoEs).

After analysing the performed CCC DoEs, the effect of L/S ratio upon granule size and shape was found to be more important compared to MFR and SS (see results section). Therefore, MFR and SS were fixed at 20 kg/h and 675 rpm (i.e., no DoE was performed) for the formulation containing anhydrous theophylline 200M (T50). Hence, 28 experiments (7 experiments at 4 TSG compartments) were performed for T50. In order to study the effect of L/S ratio on the API and binder liquid distribution of the granules for formulations 2R50 and 4R50, experiments were performed at the lowest and highest L/S ratio while keeping MFR and SS fixed at 20 kg/h and 675 rpm (see Section 3.5.2). The CCC DoEs were set up and analyzed using MODDE Pro 13.0 (Umetrics, Sartorius Stedim Biotech, Malmö, Sweden).

3.5 Granule characterization

3.5.1 Granule size and shape

A dynamic image analyser (QICPIC particle size analyzer, Sympatec, Clausthal-Zellerfeld, Germany) equipped with a vibrating feeding unit and dry dispersion unit was used to measure the granule size and shape distribution of the collected granule samples for each DoE experiment and at each compartment. Samples of 10 g were measured in triplicate. The equivalent projected circle (EQPC) diameter was calculated for each particle to derive the granule size distribution (GSD). The GSD was expressed as the volume fraction distribution over a grid consisting of a total of 35 bins, spaced as a geometric sequence between 8.46 µm and 6765.36 µm. From each measurement, the fraction of oversized granules (>4000 µm) and fines was calculated. The fraction of fines was calculated as the volume percentage of particles smaller than the d0.90_F (i.e., 90% cumulative under-size fraction of the size distribution of the formulation preblend). The granule shape distribution was determined by calculating the aspect ratio (AR) for each particle, which measures the elongation of the granules. It is the ratio of the smallest over the largest diameter of the granule. Aspect ratio varies from below 0.5 for elongated, rod shaped particles, to approximately 1 for perfect spheres.

3.5.2 Binder liquid and API distribution

A detailed description of the experimental setup used to obtain the binder liquid and API distribution of the collected granules can be found in a recent paper published by Ghijs et al. (2021). Here, a summary of the used method will be given.

Binder liquid and API distribution measurements were performed by dispersing the collected granules on a conveyer belt (ENP, Hjälteby, Sweden), which transports the granules underneath a near-infrared chemical imaging (NIR-CI) camera (VLNIR with OLES56 lens, Specim, Finland) receiving the reflected photons emitted by a halogen lamp. The hyperspectral imaging device was used in push-broom configuration, providing a row of spectra (line scan) of 2.7 cm wide of the surface in each movement. As one line scan contained 320 pixels, each spectrum captured a width of 84.375 µm. The frame rate was set at 88 Hz and the belt speed was chosen to be 13.33 cm s^{-1}, which gave a length for each line scan of 274 µm.

To evaluate the effect of the maximum solubility (S_{max}) of the API on the distribution of the API and binder liquid in the granules, formulations 2R50 and 4R50 were compared which contained a freely soluble and practically insoluble API, respectively (Table 1). The distribution of the API in the granules collected at the intermediate TSG compartments (Fig. 1) for formulations 2R50 and 4R50 was assessed by applying Principal Component Analysis (PCA) in the spectral region between 1100 and 1650 nm. Therefore, a PCA model was constructed for 2R50 and 4R50 at each TSG compartment. To measure the binder liquid concentration in the granules, a calibration model was trained that can link the spectral data to the water content in the

granules. Wet granules were collected in C6 for 2R50 and 4R50 at the highest L/S ratio (Table 2), while the MFR and SS were kept fixed at 20 kg/h and 675 rpm. Next, these granules were dried in open air for different times to obtain granule samples of different moisture content (n = 15) to be measured with the NIR-CI setup and the reference method. The reference method for moisture content determination involved the loss-on-drying (LOD) method (Council of Europe, 2008) by oven drying for 24 hours at 90°C. The prepared granule samples of different moisture content were stored in a zipper bag for one hour to allow the material inside the bag to reach equilibrium with the air in the bag and thus achieving a more homogeneous distribution in moisture content of the granules. The zipper bags were then stored on a layer of dry ice before the NIR-CI and LOD measurements were performed. This was performed to take into account the cooling step for the measurement of the actual granules at different TSG compartments. The temperature of water alters hydrogen bonding configurations and hence its absorbance spectrum (Gowen et al., 2013). From each zipper bag, five samples were taken and measured by NIR-CI and one sample was taken for the LOD reference measurement.

The spectra were pre-processed to remove interferences of unwanted information. First, dead pixels were removed. Second, noise was removed from the spectra by Savitzky-Golay smoothing with a polynomial degree of 2 and a window size of 11 (Savitzky and Golay, 1964). Third, standard normal variate (SNV) correction was used to eliminate baseline offset variations, which can be caused by scatter differences between samples due to differences in granules size and morphology. SNV transformation subtracted each spectrum by its own mean and divides it by its own standard deviation. Hence, each spectrum was centred around zero and had a standard deviation of 1. Finally, pixels containing spectral information from both background and granules were removed by applying a Classical Least Squares (CLS) algorithm which determines the amount of background contribution in each pixel. Pixels that contain more background contribution than the threshold value of 0.3 were classified as background and removed. Of the remaining pixels, the background contribution was subtracted in order to uniformise the material spectra as well as possible.

After the spectra were pre-processed, an elastic net regression (ENR) model was trained that predicts the binder liquid concentration of the granules based on the absorption spectra. Accordingly, the spectra of the granules (matrix X) were correlated with the LOD measurements (matrix Y). Multicollinearity can be an issue when performing regression on this dataset. It results from spectral variables (i.e., wavelengths) being linearly related to each other, resulting in less statistically robust models. ENR is a regularisation technique that imposes penalties on the regression coefficients to punish model complexity and multicollinearity (Zou and Hastie, 2005).

The quality of the ENR model was assessed by means of the coefficient of determination (R^2) and root mean squared error (RMSE)-values (Equations 1 and 2), calculated by:

$$R^2 = 1 - \frac{\sum_{n=1}^{N}(y_n - \hat{y}_n)^2}{\sum_{n=1}^{N}(y_n - \bar{y})^2} \quad (1)$$

$$RMSE = \sqrt{\frac{\sum_{n=1}^{N}(y_n - \hat{y}_n)^2}{N}} \quad (2)$$

where y_n, $\hat{y}_n$, and $\bar{y}$ denote the observed value, the value calculated by the calibration model, and the mean of the observations, respectively. The subscript n represents the number of each experiment and N the total number of experiments. Hence, the R^2 and RMSE-values were calculated by comparing the predicted moisture content by the calibration model $\hat{y}_n$ to the measured value y_n. The measured value y_n was left out of the calibration model to calculate the moisture content $\hat{y}_n$.

Finally, the binder liquid and API distribution of the granules of formulations 2R50 and 4R50 was measured. Granules were collected at the intermediate TSG compartments (Fig. 1) applying a low and high L/S ratio (Table 2 and Section 3.4). Granules were sieved into three different fractions (< 180 µm, 180 – 300 µm and >300 µm) and rapidly cooled by pouring into plastic trays which were put on dry ice to avoid evaporation between production and measurement of the granules. NIR-CI measurements were repeated 15 times for size fraction >300 µm and 5 times for size fractions <180 µm and 180 – 300 µm.

All spectral data processing, PCA analysis and ENR was performed using the HYPER-Tools package in MATLAB (MathWorks®, Natick, Massachusetts, USA), version R2019a.

3.6 Evaluation of the granule size and shape evolution

3.6.1 PCA of the granule size distributions at intermediate TSG compartments

With the aim of evaluating the granule size distribution change along the length axis of the TSG and compare this between the different formulations, the granule size distribution dataset was subjected to principal component analysis (PCA) to reduce the volume fraction distribution over 35 granule size bins to a limited number of overarching properties (i.e., the principal components). The X data-matrix consisted of 796 observations (i.e., number of TSG experiments, see Section 3.4) and 35 variables (i.e., number of granule size bins). The PCA analysis was performed using the Python packages (scikit-learn).

3.6.2 Effect of formulation properties and process parameters on granule size and shape evolution

Partial least squares (PLS) regression was used to evaluate the effect of the formulation blend particle size, formulation drug load, API properties, applied TSG parameters (L/S ratio, SS and MFR) (X data-matrix) on the change in fraction of fines and oversized granules in each TSG compartment (C1, KZ1, KZ2 and SCE) (Y data-matrix). The Y data-matrix was calculated for the experiments described in Sections 3.3, 3.4, and 3.5.1. These were obtained by subtracting the fraction of fines and oversized in the preblend from C1, C1 from C3, C3 from C5, and C5 from C6, respectively. Separate PLS models were trained correlating the X data-matrix with the granule size change at C1 (Y_1 data-matrix), KZ1 (Y_2 data-matrix), KZ2 (Y_3 data-matrix) and SCE (Y_4 data-matrix), respectively. The X data-matrix consisted of 55 variables (7 particle size properties of the formulation blends, 44 API properties (Table 3), the drug load, and 3 TSG parameters) and 199 observations (i.e., number of experiments performed at each TSG compartment, see Section 3.4). Each Y data-matrix consisted of 2 variables (i.e., change in fraction of fines and oversized granules) and 199 observations. The values of the X data-matrix were pre-treated prior to PLS regression via unit variance (UV) scaling and mean-centering. Observations that had a large influence on the model (high Hoteling's T^2) but that were not well captured (high squared prediction error (SPE)), in spite of their influence, were removed from the database (Y data-matrix) as outliers. The numbers of outliers were 7, 6, 3, and 10 for C1, KZ1, KZ2, and SCE, respectively. In order to avoid overfitting and include only the material properties and process parameters that were relevant, the X variables with no significant correlation were excluded during the development of the PLS models.

For the evaluation of the effect of the formulation properties and TSG process parameters on the granule shape evolution, a similar PLS analysis as for granule size was performed. However, since the AR of the preblend was not available, only the change in AR in KZ1, KZ2 and SCE was calculated. Separate PLS models were trained for these three compartments. A fourth PLS model was trained correlating the X data-matrix with the AR of the granules in C1. The change in AR for each experiment in the dataset was calculated as the average change in AR of the particles in the fines fraction (upper size limit based on d0.90_F), yield and

oversized fraction (>1500 µm), respectively. 1500 µm instead of 4000 µm was used as upper limit of the yield fraction because the AR was only measured for particles up to 2696 µm.

The PLS models were developed using the Python packages (scikit-learn).

4. Results and discussions

4.1 Granule size distribution evolution

In TSWG, the formulation preblend was transformed into granules by adding a binder liquid and the use of co-rotating screws. A representative example of this process is given in Fig. 2 (granule size distributions) and Table 4 (d-values) for H50 applying the lowest and highest L/S ratio (Table 2). During the wetting phase (preblend to C1), preblend particles interacted with the binder liquid, leading to the formation of immersion type of nuclei (big, wet, loose agglomerates or nuclei of powder) (Vercruysse et al., 2015). This was reflected by a decrease in the size peak representing un-granulated material (<300 µm), and compensated by a strong increase in the fraction of large agglomerates (>3000 µm). Next, in KZ1 (from C1 to C3), un-wetted particles (<300 µm) were captured into granules and the large agglomerates made in the wetting zone (>3000 µm) were broken and consolidated by the kneading elements. In KZ2 (C3 to C5) at high L/S ratio, further granule aggregation took place, leading to a shift to the larger sizes of the initial distribution. In KZ2 at low L/S ratio, there was insufficient amount of binder liquid to promote coalescence between individual granules and breakage of the large granules (>3000 µm) took place. In SCE, large granules were broken up leading to a reduction in the fraction of large particles and an increase in the amount of fines (<300 µm).

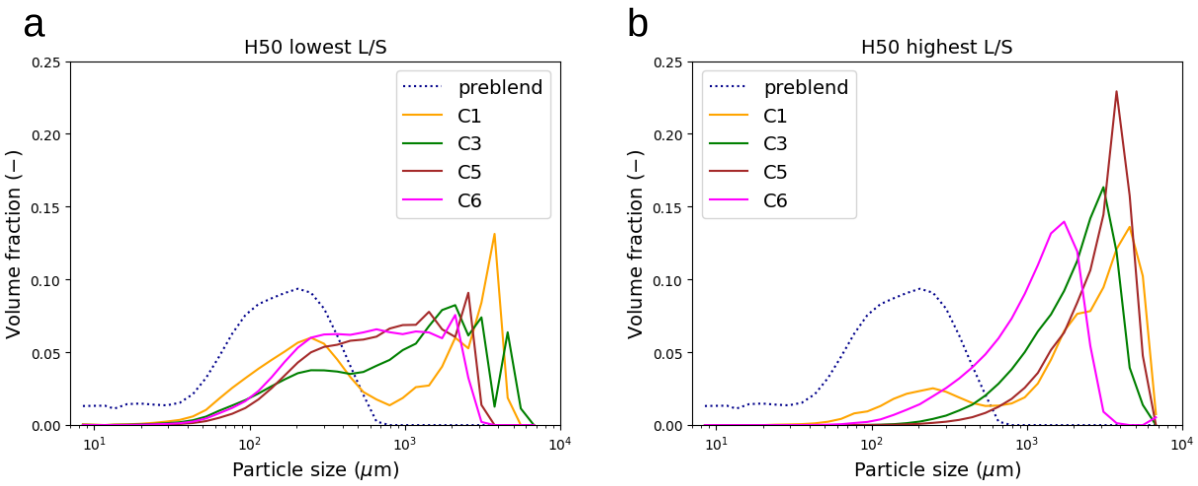

Fig. 2. Particle size distributions for preblend and granules collected in the wetting zone (C1), after the first kneading zone (C3), after the second kneading zone (C5) and at the granulator outlet (C6) for formulation H50 using the lowest (a) and highest L/S ratio (b) (Table 2).

Table 4. Overview of d-values for preblend and granules for formulation H50.

Compartment	d10 (µm)	d50 (µm)	d90 (µm)
Lowest L/S			
Preblend	31.42	132.87	324.47
C1	92.70	493.16	3329.43
C3	135.39	999.59	2955.19
C5	161.52	682.23	2132.14
C6	136.49	524.36	1783.46
Highest L/S			
Preblend	31.42	132.87	324.47
C1	199.71	2332.43	4659.61
C3	699.35	2034.27	3441.47
C5	1089.31	2872.17	4220.78
C6	330.03	1101.98	1984.09

The absolute change in the fraction of fines (based on the formulation preblends d90) and oversized (>4000 µm) granules in the intermediate TSG compartments (C1, KZ1, KZ2 and SCE) of the complete dataset (i.e., 796 TSG experiments, see Section 3.4) is shown by the violin plots in Fig. 3. These violin plots show a kernel density estimation of the distribution of the change in fines and oversized fraction for the complete dataset.

The amount of fines were strongly reduced for all formulations in C1 (Fig. 3, left). For a large part of the experiments, the fine fraction was reduced by more than 80% and thus the collected granules contained less than 20% of fines. In KZ1, the amount of fines were further decreased for most of the experiments because unwetted powder particles were combined with binder liquid into granules by the kneading elements. The change of the fines fractions was smaller in KZ2. Yet, for most of the experiments, there was a further reduction in the fraction of fines due to layering around already formed granules. In the SCE, the amount of fines slightly increased for most of the experiments because of the consolidation and breakage of oversized particles into smaller particles.

In Fig. 3 (right), the fraction of oversized particles was increased in C1 due to the formation of large agglomerates. The large agglomerates from C1 were broken-up and consolidated by the kneading elements in KZ1, as shown by the strong reduction in oversized fraction for most of the experiments. In KZ2, the amount of oversized granules increased when applying a high L/S ratio but breakage of large granules and hence a reduction in the oversized fraction was observed when using a low L/S ratio (Fig. 2 and KZ2 in Fig. 3). Whereas consolidation and breakage resulted in a reduction in the oversized particles in the SCE, some formulations such as 3F50 showed an increase in very large granules due to the very high S_{max} of the API (see Section 4.1.1).

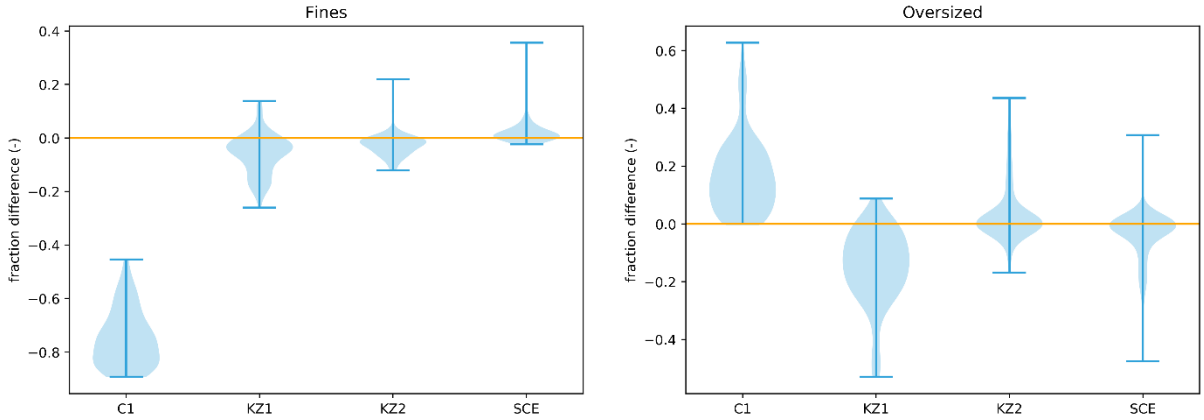

Fig. 3. Violin plots of the change in fines (left) and oversized (right) fraction in C1, KZ1, KZ2 and SCE.

4.1.1 PCA of the granule size distributions at intermediate TSG compartments

To characterize the granule size distributions for different compartments of the TSG, PCA was applied on the granule size distribution dataset obtained for each formulation at each TSG compartment. Since it is difficult to characterize and interpret a large number of granule size distributions that contain high-dimensional data, dimensions of the distribution dataset were reduced to two principal components (PCs) by PCA. The resulting loadings and score plots are shown in Fig. 4-a and Fig. 4-b, respectively. The first principal component (PC1) as well as the second principal component (PC2) described the change in small and large particles. The first principal component (PC1) had strong positive loadings for small particles (70 µm) and strong negative loadings for large particles (1000 µm) whereas the second principal component (PC2) had strong negative loadings for medium-sized particles (400 µm) and

strong positive loadings for very large particles (4000 µm). From the score plot (Fig. 4), it can be seen that the granules collected in C1 contained a high amount of ungranulated powder (high PC1 scores) as well as a high amount of large agglomerates (high PC2 score). When granules were transported towards the TSG outlet (from C1 to C6), the amount of very large particles decreased (decreasing PC2 scores) because of the consolidation and breakage in the subsequent kneading zones and size control elements section. Furthermore, the ungranulated powder from C1 was captured into granules (decreasing PC1 score) by the shear and compression forces of the kneading elements.

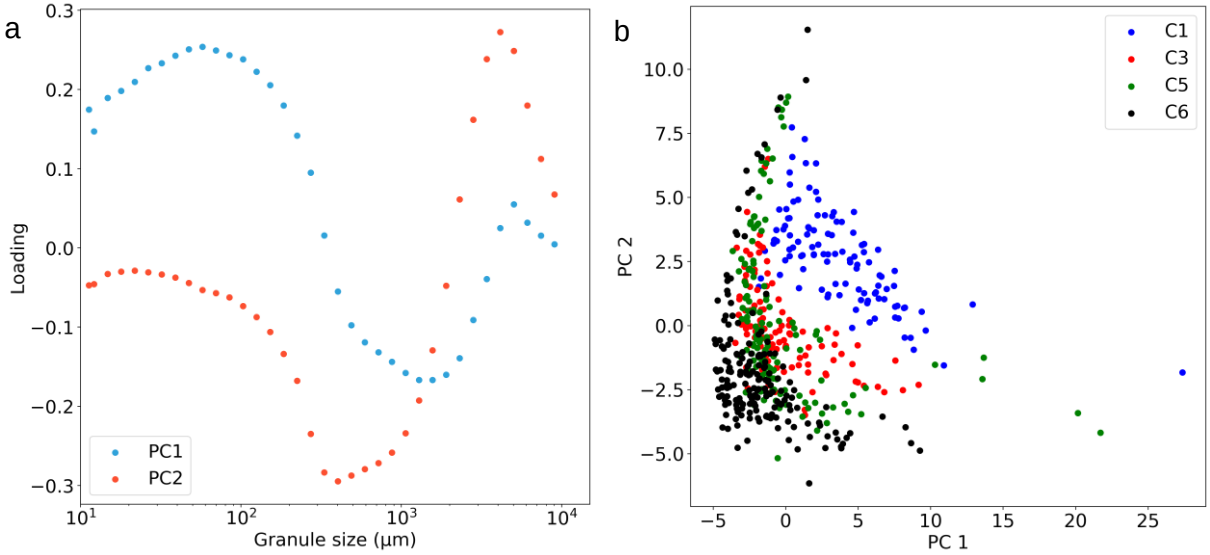

Fig. 4. Loadings (a) and score (b) plot of the PCA model developed using the granule size distribution dataset.

Next, separate PCA models were constructed for the granule size distribution data obtained at each TSG compartment to compare the granule size evolution between the different formulations. Four PCA models each consisting of two PCs were obtained (see Fig. 5).

Divergent granule size distributions were observed for 4F50 in C1 and C5 (high PC1 and PC2 scores) as well as for 3F50 in C6 (low PC1 scores and high PC2 scores). Because of the poor wettability of 4_f (CA1 = 129.3°), the binder liquid was repelled by the hydrophobic API particles and granules containing a high amount of fines (high PC1 score) were obtained in C1 and C5 for 4F50. Due to the higher solubility (S_{max}) and dissolution rate (DR) of 3_f compared to the other APIs, granules for 3F50 (orange dots in Fig. 5) in C6 were collected containing a very high amount of oversized particles (high PC2 score) and a low amount of fines (low PC1 score) when applying a high L/S ratio. The high solubility (S_{max}) promoted the dissolution of a large fraction of API particles and hence the formation of numerous strong liquid bridges, which resulted in the creation of oversized granules.

These findings for formulations 4F50 and 3F50 support the results of a previous publication (Peeters et al., 2023a). The screw configuration and excipient base that was used in this study was not suitable for formulations containing 50% w/w of an API with a very high solubility (S_{max}) (i.e., 3_f) or 50% w/w of an API with a very poor wettability (CA1) and small particle size (i.e., 4_f). In order to allow granulation of these formulations, the SCE in the screw configuration could be replaced by two chopper elements for formulation 3F50 because granule size distributions were similar until C5. In case of formulation 4F50, where granule size distributions were already different in C1, the API concentration in the powder blend could be decreased for formulation 4F50.

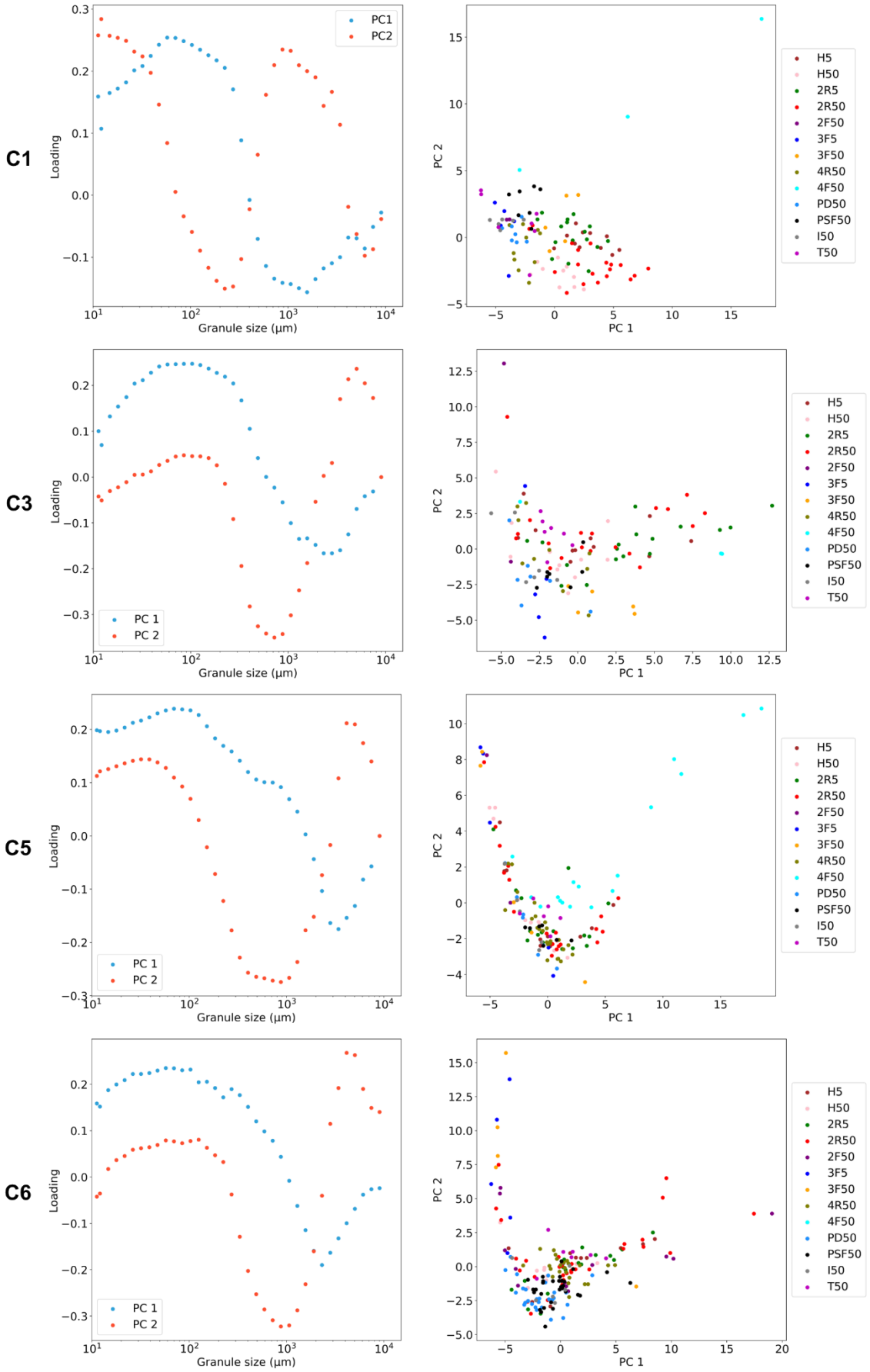

Fig. 5. Loadings (left) and score (right) plot of the PCA models developed using the granule size distribution data from the intermediate TSG compartments (C1, C3, C5 and C6).

4.1.2 Effect of formulation properties and process parameters on granule size evolution

For each TSG compartment (C1, C3, C5 and C6), a two-latent variable (LV) PLS model was fit to the data as R^2X and R^2Y only slightly increased when a third LV was added. Furthermore, adding a third LV complicated the physical interpretation of the results.

The initial X data-matrix consisted of 55 variables (i.e., particle size properties of the formulation blends, API properties, the drug load, and TSG parameters) and 199 observations (i.e., number of experimental runs performed) for each compartment (see Section 3.6.2). Based on the PCA plots (see Section 4.1.1), data of formulations 4F50 and 3F50 were excluded from the data set. After excluding outliers and non-relevant input variables (see Section 3.6.2), the number of variables and observations used for the model development became 32 variables and 102 observation (C1), 20 variables and 103 observations (C3), 28 variables and 103 observations (C5), and 30 variables and 87 observations (C6). L/S ratio was found to have a more important effect on the change in granule size (i.e., fraction of fines and oversized granules) compared to the other process parameters MFR and SS, which confirms the observations in a previous study from Verstraeten et al. (2017). Hence, only L/S ratio was retained as a TSG process parameter in the X data-matrix of the PLS models finally, and this finding could drive a reduction of experimental tests in the future development.

The effect of the raw material properties and L/S ratio upon the change in fines and oversized particles was studied in more detail by interpreting their loadings for each LV. The loadings plots of the different PLS models are provided in Fig. 6. In addition, the formulation properties that were retained in the final PLS models are shown in the Variable Importance for the Projection (VIP) plots (Fig. 17 in Appendix B). These were created to highlight the most influencing raw material properties and process parameters in the PLS models and thus with the largest effect on the change in granule size in each TSG compartment.

In C1, the L/S ratio was found to have a more important impact on changing the fine and oversized particle fraction compared to the material properties (see Fig. 17-a in Appendix B). Increasing the L/S ratio makes the binder liquid occupy more pores of the powder bed, which further leads to the increase of the number of nuclei that are created. Therefore, adding more binder liquid to C1 decreases the fraction of ungranulated material and increases the fraction of oversized particles.

From the material properties, particle size, flow, water binding capacity, and contact angle (CA1) were identified as the most impacting parameters on granule particle size. When the particle size (e.g., d0.9_F) increased, a stronger increase in the amount of coarse granules was observed. This correlation between the particle size related properties and the change in oversized particles is illustrated in Fig. 6. This effect of the initial particle size on the increase in the amount of coarse particles was demonstrated by comparing the change in particle size distribution inside C1 between formulations 4R50 and 4F50, which contained 50% w/w of a coarse (4_r) and fine (4_f) grade of the same API. Experiments were performed using identical TSG process settings for the two formulations (Fig. 11, Appendix A). The preblend of these two hydrophobic formulations consisted of a mixture of hydrophilic excipient particles and hydrophobic API particles. In the wetting compartment, the hydrophilic particles are preferentially nucleated constituting a core. The hydrophobic API particles are attaching to this core by layering due to the excess amount of binder liquid that is available (Hapgood et al., 2009). When the API PSD and thus the preblend PSD was larger (4R50), the particles attaching to the core were larger and consequently the size of the agglomerates increased (Fig. 11, Appendix A).

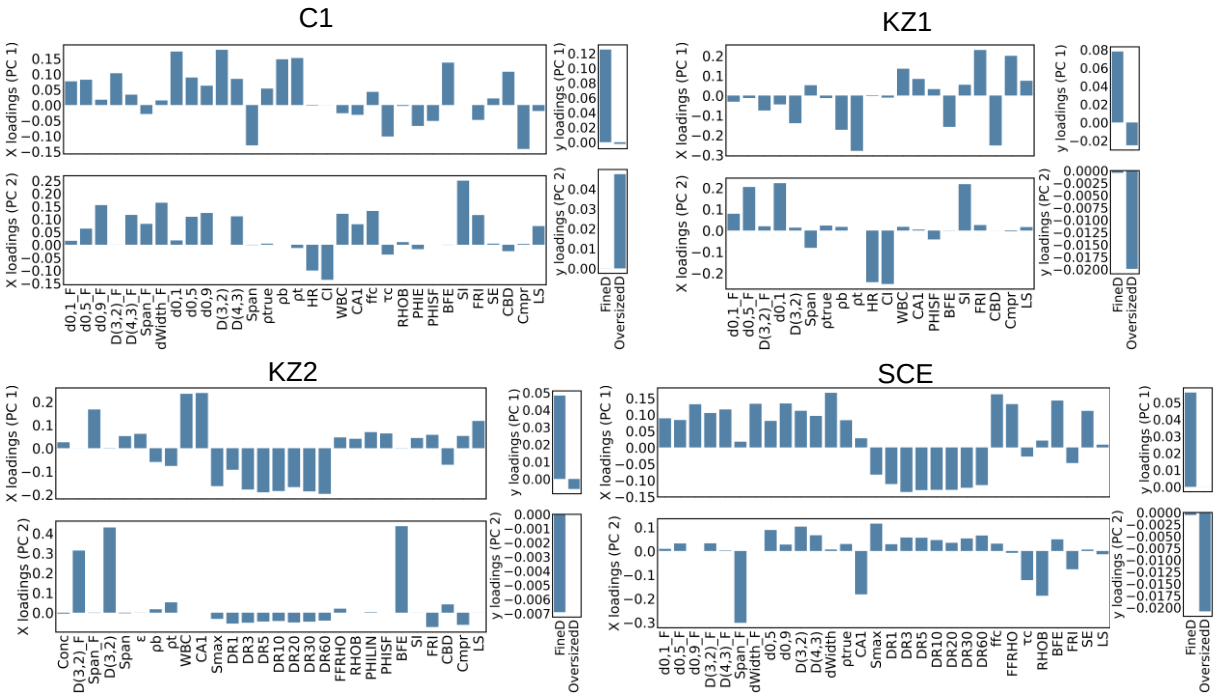

Fig. 6. Loading plots of PLS models for the change in granule size in the wetting compartment (C1), the first kneading zone (KZ1), the second kneading zone (KZ2) and the size control elements (SCE).

Formulations with lower wettability of the API (i.e., higher CA1) presented a larger increase in the fraction of coarse granules in C1, which can be derived from the loadings plot in Fig. 6. This effect of wettability (CA1) on the size change is displayed in Fig. 12 (Appendix A). H50 and 4R50 had a similar preblend particle size distribution (dotted lines) but a higher fraction of coarse particles were obtained for 4R50 in C1. Since the wettability of 4_r (CA1 = 129.3°) was poorer than that of HCT (CA1 = 72.3°), hydrophobic formulations (4R50) required higher amounts of binder liquid for granulation compared to H50 (Table 2) during TSWG. Therefore, more particles can attach to the initial core in C1 creating larger agglomerates if the wettability of the API is lower.

In KZ1, size-related properties (e.g., d0.1), density (e.g., ρt), flow-related properties (e.g., BFE), and wettability properties (e.g., CA1) were impacting the change in granule size (Fig. 17-b in Appendix B). The API particle size (d0.1) was inversely correlated to the increase in oversized particles (i.e., when the initial API particle size (d0.1) was larger, there was a stronger reduction in coarse particles) (KZ1 in Fig. 6). This is illustrated by comparing the change in granule size between formulations 4R50 and 4F50 (Fig. 13, Appendix A), where there was a larger decrease in the amount of oversized particles for 4R50 when applying the same TSG process parameter settings. This effect of the API particle size could be explained by the higher fraction of oversized granules that were obtained in C1 and subsequently entered KZ1 for 4R50 compared to 4F50.

Formulations containing an API with a lower wettability (higher CA1) were characterized by a smaller reduction or even increase in the amount of fines inside KZ1 due to the poorer interaction between the binder liquid and powder particles (Fig. 14, Appendix A). While H50 ($CA1_{HCT}$ = 72.3°) showed a small decrease in fines (blue curve in Fig. 14, Appendix A), there

was almost no reduction in the amount of fines for 4R50, which contained an API with a higher CA1 (i.e., 129.3°).

Wettability properties had a more important effect on the change in granule size in KZ2 compared to C1 and KZ1 (Fig. 17-c). It could be related to the shearing effect of the kneading elements, which resulted in a good interaction between the powder particles and binder liquid, promoting the dissolution of the powder particles and creation of liquid bridges. Consequently, the interaction became stronger along with the progress of the kneading, which leads to the higher impact of water-related material properties in KZ2.

The water binding capacity (WBC) and wettability (CA1) were correlated to the increase of fines in KZ2 (KZ2 in Fig. 6). When more binder liquid was held by the powder bed (higher WBC), less was available for granulation which resulted in an increase in the amount of fines inside KZ2. A lower wettability (higher CA1) gave a poorer interaction between the powder and binder liquid in KZ2, and consequently a higher fraction of ungranulated powder in C5. A higher solubility (S_{max}) or dissolution rate (DR) resulted in a faster powder dissolution, and hence more granulated material and a smaller fines fraction inside KZ2 (i.e., S_{max} and DR were anti-correlated to the fines). This effect of the water related properties on the fines can be observed in Fig. 15 (Appendix A) where there was an increase in fines inside KZ2 for 4R50 compared to a decrease in fines for H50 (lower WBC and CA1 and higher S_{max} and DR).

In the final screw compartment (SCE), L/S had a more important effect on the size change compared to the material properties (Fig. 17-d in Appendix B). The slicing planes cut in these screw elements chop up oversized granules entering the SCE. At higher L/S, a higher amount of oversized granules exited KZ2, more granules were broken up by the SCE and thus a stronger reduction in oversized granules in the SCE was observed. Regarding material properties, particle size-related properties (e.g., d0.9) as well as flow-related (e.g., BFE) and water-related material properties (e.g., S_{max}) were important for the change in fines and oversized granules inside the SCE.

Particle size (e.g., d0.9) was correlated with fines (SCE in Fig. 6) which could be related to the larger particles giving weaker granules due to the lower number of inter-particle contact points. Hence, these granules showed a stronger increase in fines inside the SCE due to the higher degree of granule breakage. The effect of the initial particle size on the change in fines is illustrated in Fig. 16 (Appendix A). The change in granule size distribution inside the SCE when applying identical TSG settings was compared between formulations 2R50 and 2F50. When using a coarser grade of the API in the formulation (2R50), there was a stronger increase in fines inside the SCE.

4.2 Granule shape distribution

The PLS models were developed to analyze the effect of L/S ratio and material properties on the AR distribution in C1 as well as on the change in AR in KZ1, KZ2 and SCE (see Section 3.6.2 for details on the structure of the established models). The VIP plots and loading plots of the four PLS models can be found in Fig. 18 and Fig. 19, Appendix B. The impact of L/S ratio on granule shape became bigger along with the progress of granulation. In C1 and KZ1, size-related properties showed a high impact on the AR distribution because initial particle morphology is important when granulation is incomplete. In SCE, where the interaction between the powder particles and binder liquid was stronger compared to the upstream TSG compartments, water-related material properties (e.g., S_{max}) were the most important..

Based on the interpretation of the developed PLS models, the TSG process parameter L/S ratio and the solubility of the API (S_{max}) were found to have an important impact on the AR distribution in C1 as well as on the change in AR in KZ1, KZ2 and SCE. Therefore, the AR

distributions of granules collected at the intermediate TSG compartments for formulations containing a freely soluble API (2R50), a slightly soluble API (T50) and a practically insoluble API (4R50) were compared when applying the lowest and highest L/S ratio (Fig. 7 and Table 2). In general, the granules became more spherical towards the TSG outlet which agrees with the findings in previous studies (Dhenge et al., 2012; Liu et al., 2015; Verstraeten et al., 2017). The AR of the agglomerates (>1500 µm) in C1 increased with decreasing API solubility (i.e., 4R50 > T50 > 2R50 in Fig. 7). This could be explained by the higher amount of binder liquid that is required to promote granule growth for formulations containing an API with a lower solubility (i.e., higher hydrophobicity). Consequently, there is a higher availability of binder liquid at the surface of the initially wetted agglomerates which allows a higher degree of layering of un-wetted fines from the surroundings. This might increase the sphericity of the initial agglomerates.

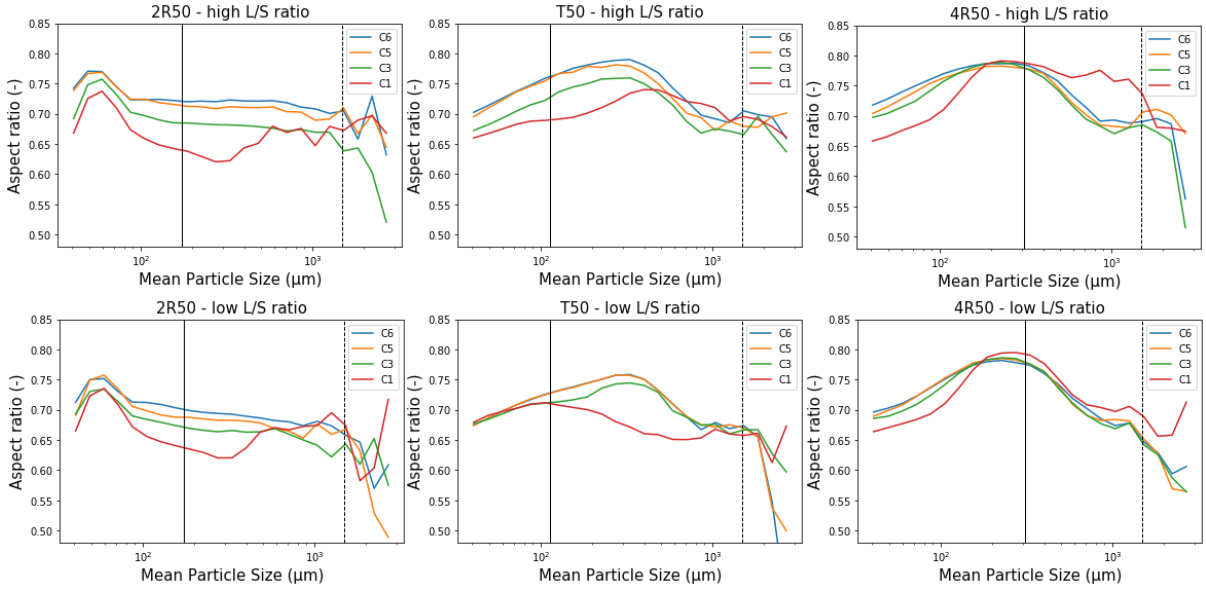

Fig. 7. Aspect ratio in function of granule size for formulations 2R50, T50 and 4R50 produced using the lowest and highest L/S ratio (Table 2). The aspect ratio is given for the intermediate TSG compartments (C1, C3, C5 and C6). The cut-off size for the fines (full line) and oversized (dotted line) are indicated.

The fines fraction (indicated by a full line in Fig. 7) consisted of ungranulated preblend particles and small granules. In KZ1 (C1 to C3 in Fig. 7), there was an increase in AR for this fraction which could be attributed to the layering of unwetted preblend particles around the initial small granules in KZ1. For some experiments at low L/S there was almost no change in AR (C1 to C3 for T50 at low L/S ratio in Fig. 7) because there was insufficient amount of binder liquid to bind ungranulated powder particles to the initial granules.

The AR of the granules in the yield fraction increased for most of the experiments in KZ1 but for hydrophobic formulations, the AR decreased due to consolidation of the large agglomerates (> 1500 µm) from C1 into smaller, more elongated particles (C1 to C3 for 4R50 in Fig. 7). The AR of the oversized granules decreased in KZ1 due to breakage and consolidation.

The introduction of granules to KZ2 (C3 to C5 in Fig. 7) led to spheronization of the initial granules by collisions between neighbouring granules or between granules and screw elements. As a result, the AR of the processed granules increased in KZ2. With increasing hydrophobicity (i.e., 4R50 > T50 > 2R50), there was a smaller increase in AR in KZ2 probably because the granules in C3 were already more spherical for hydrophobic formulations compared to hydrophilic formulations.

There was only a smaller change in the granule shape inside SCE (C5 to C6 in Fig. 7) compared to the other compartments. In general, the granule AR slightly increased. L/S ratio had a more important effect on granule shape compared to material properties (see loadings plot of the PLS model for SCE in Fig. 19, Appendix B) in this compartment. By using a higher L/S ratio, granules became more spherical inside SCE since more binder liquid was available to promote plastic deformation and spheronization of the granules.

Besides the solubility of the API (S_{max}), also other raw material properties had an impact on the granule shape evolution inside the TSG (Fig. 19, Appendix B): preblend particle size (e.g., d0.9_F) for KZ1, flow-related properties (e.g., FRI) and density (e.g., CBD) for KZ2 and flow-related properties such as ffc and HR for SCE. The effect of these properties on granule AR was expected as they had a large effect on the change in granule size inside the TSG.

4.3 Effect of formulation properties on the binder liquid and API distribution

The quality of the elastic net regression (ENR) models for the hydrophilic (2R50) and hydrophobic (4R50) formulations in terms of predictive performance was good, as can be derived from their coefficient of determination (R^2) and root mean squared error (RMSE) values. Both models can be considered quite accurate with RMSEs of 0.077 % w/w and 0.062 % w/w and R^2s of 0.761 and 0.874 for 2R50 and 4R50, respectively.

The median moisture content of the granules for different fractions (with cut-off sizes 180 µm, 300 µm, 710 µm, 1000 µm, 1400 µm, 1700 µm, 2000 µm and 3150 µm) measured by the NIR-CI method can be found in Fig. 8 and Fig. 9. Although the moisture content results for both the lowest and highest L/S ratios are presented, the observed difference in moisture content between these ratios was not substantial. This phenomenon can be attributed to the saturation limit of water binding within the granules or powder particles. As the L/S ratio increased, there was a noticeable increase in the quantity of larger granules due to the augmented availability of binder liquid, as depicted in Figs. 2 and 6. However, the moisture content of these larger granules tended to remain relatively constant. This phenomenon can be explained by the fact that granules have a maximum saturation point for water binding. Beyond this point, the additional liquid did not proportionally increase the moisture content of the granules. Instead, it led to a higher quantity of larger granules, where the moisture content is inherently higher compared to smaller granules.

The binder liquid was not homogeneously distributed over the different size classes inside C1 for 2R50 (Fig. 8a). Larger agglomerates contained a higher amount of binder liquid. During the wetting phase of hydrophilic formulations, the binder liquid can easily penetrate into the pores of the hydrophilic powder bed to form highly saturated nuclei with relatively smaller amounts of binder liquid at the edges (Kumar et al., 2014). Consequently, smaller particles that break off from the edges of the initial agglomerates contain a lower amount of binder liquid. Furthermore, initial agglomerates with a higher moisture content are stronger, more elastic, and hence have less tendency to break into smaller particles. As shown in Fig. 8, the granule moisture content in C1 increased with increasing L/S ratio for 2R50. This is because the initial agglomerates and hence also the small parts that break off contained more binder liquid.

As opposed to 2R50, the binder liquid was homogeneously distributed over the granule size classes above 300 µm for 4R50 (Fig. 8b). This can be attributed to the difference in nucleation mechanism between hydrophobic and hydrophilic formulations. During the wetting phase for hydrophobic formulations, first, hydrophilic excipient particles will preferentially be nucleated, due to the small contact angle between the hydrophilic particles and the binder liquid. Next, the remaining un-wetted hydrophobic API particles can spread over the wet agglomerates in a process of layering (Iveson et al., 2001; Charles-Williams et al., 2013). The size of the obtained agglomerates depends on the amount of hydrophobic API particles that are layered

around the hydrophilic cores but their moisture content (% w/w) remains constant. The particles for 4R50 below 180 µm contained a lower amount of binder liquid than the agglomerates >300 µm and these were probably un-wetted preblend particles ($d0.5_{4R50}$ = 105 µm). The granule moisture content for 4R50 was not impacted by the L/S ratio. By increasing the amount of binder liquid that is applied during TSWG, more hydrophobic API particles can attach to the hydrophilic core but the concentration of binder liquid inside these agglomerates remains similar.

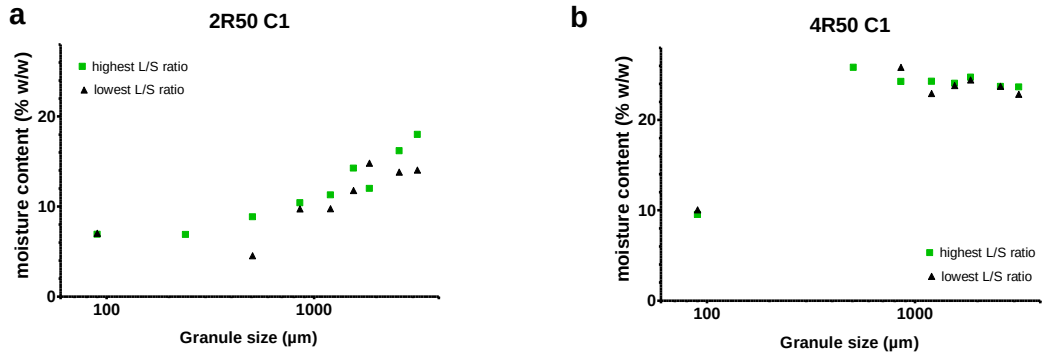

Fig. 8. Moisture content distribution of the granules collected at C1 using (a) the lowest (5.2%) and (b) the highest L/S ratio (16.0%) for the formulation 2R50, and (c) the lowest (20.0%) and (d) the highest L/S ratio (28.0%) for the formulation 4R50.

When the granules of the hydrophilic formulation (2R50) were moving through the kneading zones (C1 to C3 and C3 to C5) and SCE (C5 to C6) of the TSG, some redistribution of the binder liquid among the different size fractions took place (Fig. 9a, b). There was a small increase in the moisture content of the granules below 710 µm in KZ1 (C1 to C3) due to consolidation and breakage of the large initial agglomerates from the wetting zone that contained a high amount of binder liquid (Fig. 8a). Yet, the binder liquid remained in-homogeneously distributed in the final material (C6). This could be explained by the low amount of binder liquid that is required for hydrophilic formulations for granulation. The inner pores of the granules contained only a limited amount of liquid which was difficult to be squeezed out towards the granule surface and redistributed over the granules of the different size fractions. Furthermore, the hydrophilic particles can easily bind and hold the binder liquid which mitigated the transport of liquid from within the granule pores.

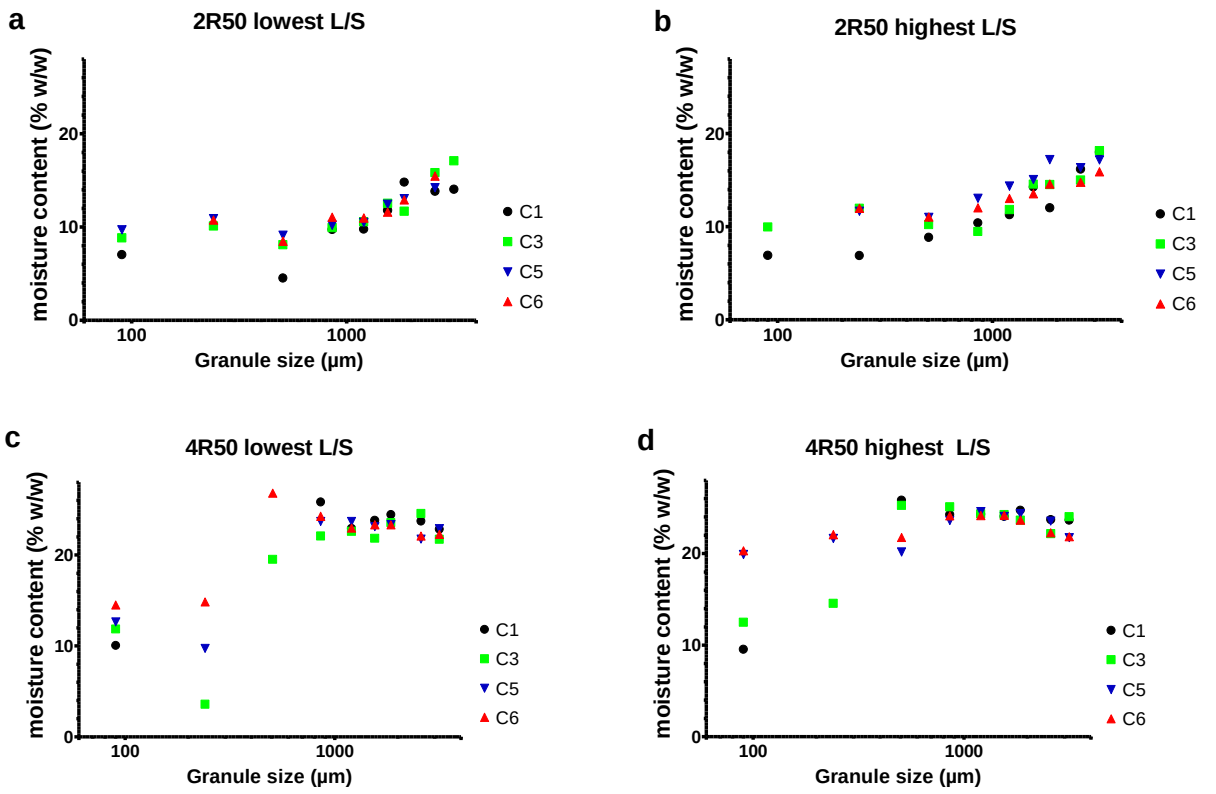

Fig. 9. Moisture content distribution of the granules collected at C1, C3, C5 and C6 using (a) the lowest (5.2%) and (b) the highest L/S ratio (16.0%) for the formulation 2R50, and (c) the lowest (20.0%) and (d) the highest L/S ratio (28.0%) for the formulation 4R50.

On the other hand, the binder liquid was homogeneously distributed among the different granule size classes at C5 for 4R50 when applying a high L/S ratio (Fig. 9d). As a higher amount of binder liquid was used compared to 2R50, it could be squeezed out from the inner pores of the large granules and redistributed over the smaller granules inside KZ2 (C3 to C5). At lower L/S ratios, the limited amount of binder liquid could not be exchanged between the different size fractions and the granulation process inside KZ2 was dominated by breakage (see Fig. 9c and the result of 4R50 in Fig. 15a).

In order to determine the distribution of API in the granules, a PCA model containing 2 PCs was constructed for each formulation and compared with the wavelength of API. PC1 correlated with the binder liquid content. The peak of PC2 of the PCA model corresponded to the wavelengths of APIs 2_r and 4_r. Therefore, a PCA score plot was created for PC2 as an index of the distribution of the API in the collected granules (Fig. 10). The distribution of PC2 scores is represented by violin plots.

The API concentration was similar across the different size fractions (<180 µm, 180 – 300 µm and >300 µm) in the different compartments of the TSG for 2R50, as shown by the PC2 scores for each size fraction centred around zero (Fig. 10a, b). As the preblend of this formulation consisted of hydrophilic API and excipient particles which both have a high affinity for the binder liquid and thus can easily be incorporated into granules, the concentration of API in the initial agglomerates (>300 µm) and ungranulated powder (<180 µm) were similar in C1. Next, the un-wetted hydrophilic API particles were readily combined with ungranulated excipient particles into granules in the subsequent kneading zones (C1 to C3, C3 to C5 and C5 to C6) and consequently the API remained equally distributed over the different size fractions in the final granules (C6).

For formulation 4R50, the size fraction 180 – 300 µm had a higher concentration of API in C1 compared to the other size fractions. It likely consisted of hydrophobic API particles (d0.5 = 238 µm) that could not attach to the initial agglomerates during the wetting phase. This confirms the nucleation mechanism hypothesis where hydrophobic API particles are layered around a hydrophilic excipient core. In KZ1 (C1 to C3), these un-wetted API particles were incorporated into granules by the shear forces of the kneading elements. Hence, the API was equally distributed across the different size fractions in the subsequent TSWG compartments C3, C5 and C6.

4.4 Toward efficient process and formulation design

Based on the results of the impacts of formulation properties and process settings on the distributions of granule size, shape, the binder liquid, and API, it was found that material properties of new APIs would determine a suitable strategy for efficient process and formulation design. In addition, the information on granule properties in the intermediate compartments allows to evaluating the effect of modifying the screw configuration (e.g. decision to use SCE).

For example, solubility of APIs is a key factor to define screw configurations and the formulation compositions. Hydrophilic APIs resulted in a strong increase in granule size caused by the SCE and a heterogeneous binder liquid distribution. It suggests that for such APIs, the application of screw configurations without SCEs as well as the improvement of a liquid addition method might lead to ideal granule sizes and a homogeneous liquid distribution. From a formulation perspective, the formulation composition should be adapted to reduce the average water solubility of its ingredients.

For APIs with very low water solubility, a high amount of fines was obtained during granulation for high dose formulations. This observation was related to the poor interaction between the binder liquid and API particles. It might be necessary to decrease the drug load or optimize the formulation composition for such APIs. Homogeneous liquid distributions can be attained mainly by adjusting L/S ratio for hydrophobic APIs.

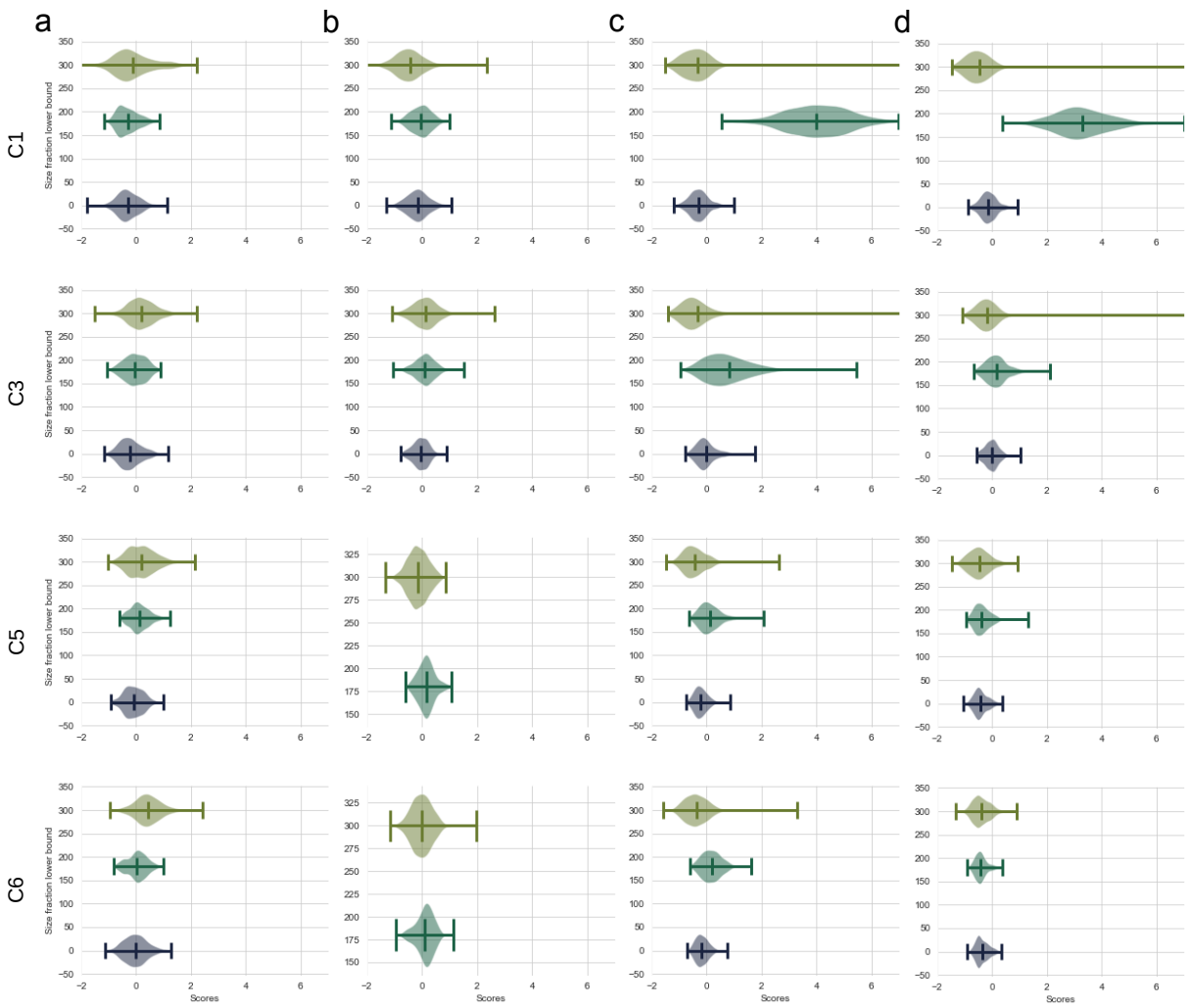

Fig. 10. PC2 score plots of the PCA models for 2R50 (a and b) and 4R50 (c and d) showing the distribution of API over the different size fractions (<180 µm, 180 – 300 µm and >300 µm) at the intermediate TSG compartments (C1, C3, C5 and C6) when using the lowest (a and c) and highest (b and d) L/S ratio.

5. Conclusion

In this study, the impact of formulation properties (i.e., API properties, formulation blend particle size and drug load) and the process parameters on formation of the granule in continuous TSWG was evaluated. Blends of APIs with very divergent physico-chemical properties with a fixed excipient base and varying drug load were processed on the TSG. Granules were characterized along the length of the TSWG barrel in terms of granule size, shape and distribution of granulation liquid and API. This research study obtained detailed information about the impact of a large number (i.e., 53) of formulation properties on the change in granule size and shape at the intermediate compartments of the TSG. NIR-CI was applied for the first time to study the effect of formulation properties on the binder liquid and API distribution along the length of the TSG barrel.

The change in granule size was the largest in the wetting compartment and the first kneading zone because of the creation and breakage, respectively, of large agglomerates. L/S ratio was the only TSG process parameter impacting the granule size and shape evolution. Flow-, size-, density- and water-related material properties had an important effect on the granule size and shape evolution at each of the intermediate TSG compartments. For a hydrophilic and

hydrophobic formulation, binder solution distribution over the different granule size fractions was compared and found to be different. Homogeneous distribution of the binder solution at the outlet of the granulator was observed just for the hydrophobic formulation and at high L/S ratio. The distribution of the API in the granules in the wetting compartment was different between formulations, yet it was always homogeneously distributed over the different granule size fractions at the TSG outlet.

References

Barrera Jiménez, A.A., Matsunami, K.K., Ghijs, M., Van Hauwermeiren, D., Peeters, M., Stauffer, F., De Beer, T., Nopens, I., 2023a. Model development and calibration of two-dimensional population balance model for twin-screw wet granulation based on particle size distribution and porosity. Powder Technol. 419, 118334. https://doi.org/10.1016/j.powtec.2023.118334

Barrera Jiménez, A.A., Matsunami, K.K., Van Hauwermeiren, D., Peeters, M., Stauffer, F., dos Santos Schultz, E., Kumar, A., De Beer, T., Nopens, I., 2023b. Linking material properties to 1D-PBM parameters towards a generic model for twin-screw wet granulation. Chem. Eng. Res. Des. 193, 713–724. https://doi.org/10.1016/j.cherd.2023.04.009

Charles-Williams, H., Wegeler, R., Flnore, K., Feise, H., Hounslow, M.J., Salman, A.D., 2013. Granulation behaviour of increasingly hydrophobic mixtures. Powder Technol. 238, 64–76. https://doi.org/10.1016/J.POWTEC.2012.06.009

Council of Europe, 2008. Eur Pharmacopoeia, 7th ed. Strasbourg.

Dhenge, R.M., Cartwright, J.J., Hounslow, M.J., Salman, A.D., 2012. Twin screw granulation: Steps in granule growth. Int. J. Pharm. 438, 20–32. https://doi.org/10.1016/J.IJPHARM.2012.08.049

FDA, 2004. Guidance for Industry PAT - A Framework for Innovative Pharmaceutical Development, manufacturing, and Quality Assurance.

Fonteyne, M., Vercruysse, J., De Leersnyder, F., Van Snick, B., Vervaet, C., Remon, J.P., De Beer, T., 2015. Process Analytical Technology for continuous manufacturing of solid-dosage forms. TrAC - Trends Anal. Chem. 67, 159–166. https://doi.org/10.1016/j.trac.2015.01.011

Ghijs, M., Vanbillemont, B., Nicolaï, N., De Beer, T., Nopens, I., 2021. Two-dimensional moisture content and size measurement of pharmaceutical granules after fluid bed drying using near-infrared chemical imaging. Int. J. Pharm. 595, 120069. https://doi.org/10.1016/j.ijpharm.2020.120069

Gowen, A.A., Amigo, J.M., Tsenkova, R., 2013. Characterisation of hydrogen bond perturbations in aqueous systems using aquaphotomics and multivariate curve resolution-alternating least squares. Anal. Chim. Acta 759, 8–20. https://doi.org/10.1016/J.ACA.2012.10.007

Hapgood, K.P., Farber, L., Michaels, J.N., 2009. Agglomeration of hydrophobic powders via solid spreading nucleation. Powder Technol. 188, 248–254. https://doi.org/10.1016/J.POWTEC.2008.05.004

Iveson, S.M., Litster, J.D., Hapgood, K., Ennis, B.J., 2001. Nucleation, growth and breakage phenomena in agitated wet granulation processes: a review. Powder Technol. 117, 3–39. https://doi.org/10.1016/S0032-5910(01)00313-8

Kourti, T., Lepore, J., Liesum, L., Nasr, M., Chatterjee, S., Moore, C.M. V, Korakianiti, E., 2014. Scientific and Regulatory Considerations for Implementing Mathematical Models in the Quality by Design (QbD) Framework. Pharm. Eng. 34, 1–21.

Kumar, A., Gernaey, K. V., Beer, T. De, Nopens, I., 2013. Model-based analysis of high shear wet granulation from batch to continuous processes in pharmaceutical production – A critical review. Eur. J. Pharm. Biopharm. 85, 814–832. https://doi.org/10.1016/J.EJPB.2013.09.013

Kumar, A., Vercruysse, J., Bellandi, G., Gernaey, K. V., Vervaet, C., Remon, J.P., De Beer,

T., Nopens, I., 2014. Experimental investigation of granule size and shape dynamics in twin-screw granulation. Int. J. Pharm. 475, 485–495. https://doi.org/10.1016/j.ijpharm.2014.09.020

Lee, S.L., O'Connor, T.F., Yang, X., Cruz, C.N., Chatterjee, S., Madurawe, R.D., Moore, C.M.V., Yu, L.X., Woodcock, J., 2015. Modernizing Pharmaceutical Manufacturing: from Batch to Continuous Production. J. Pharm. Innov. 10, 191–199. https://doi.org/10.1007/s12247-015-9215-8

Li, H., Thompson, M.R., O'Donnell, K.P., 2014. Understanding wet granulation in the kneading block of twin screw extruders. Chem. Eng. Sci. 113, 11–21. https://doi.org/10.1016/J.CES.2014.03.007

Li, J., Pradhan, S.U., Wassgren, C.R., 2019. Granule transformation in a twin screw granulator: Effects of conveying, kneading, and distributive mixing elements. Powder Technol. 346, 363–372. https://doi.org/10.1016/J.POWTEC.2018.11.099

Liu, Y., Thompson, M.R., O'Donnell, K.P., 2015. Function of upstream and downstream conveying elements in wet granulation processes within a twin screw extruder. Powder Technol. 284, 551–559. https://doi.org/10.1016/J.POWTEC.2015.07.011

Mundozah, A.L., Cartwright, J.J., Tridon, C.C., Hounslow, M.J., Salman, A.D., 2019. Hydrophobic/hydrophilic powders: Practical implications of screw element type on the reduction of fines in twin screw granulation. Powder Technol. 341, 94–103. https://doi.org/10.1016/J.POWTEC.2018.03.018

Peeters, M., Barrera Jiménez, A.A., Matsunami, K.K., Van Hauwermeiren, D., Stauffer, F., Arnfast, L., Vigh, T., Nopens, I., De Beer, T., 2023a. Exploring the effect of raw material properties on continuous twin-screw wet granulation manufacturability. Int. J. Pharm. 645, 123391. https://doi.org/10.1016/j.ijpharm.2023.123391.

Peeters, M., Barrera Jiménez, A.A., Matsunami, K.K., Stauffer, F., Nopens, I., De Beer, T., 2023b. Evaluation of the influence of material properties and process parameters on granule porosity in twin-screw wet granulation. Int. J. Pharm. 641, 123010. https://doi.org/10.1016/j.ijpharm.2023.123010

Savitzky, A., Golay, M.J.E., 1964. Smoothing and Differentiation of Data by Simplified Least Squares Procedures. Anal. Chem. 36, 1627–1639. https://doi.org/10.1021/ac60214a047

Van Hauwermeiren, D., Verstraeten, M., Doshi, P., am Ende, M.T., Turnbull, N., Lee, K., De Beer, T., Nopens, I., 2018. On the modelling of granule size distributions in twin-screw wet granulation: Calibration of a novel compartmental population balance model. Powder Technol. 341, 116–125. https://doi.org/10.1016/j.powtec.2018.05.025

Vercruysse, J., Peeters, E., Fonteyne, M., Cappuyns, P., Delaet, U., Van Assche, I., De Beer, T., Remon, J.P., Vervaet, C., 2015. Use of a continuous twin screw granulation and drying system during formulation development and process optimization. Eur. J. Pharm. Biopharm. 89, 239–247. https://doi.org/10.1016/j.ejpb.2014.12.017

Verstraeten, M., Van Hauwermeiren, D., Lee, K., Turnbull, N., Wilsdon, D., am Ende, M., Doshi, P., Vervaet, C., Brouckaert, D., Mortier, S.T.F.C., Nopens, I., Beer, T. De, 2017. In-depth experimental analysis of pharmaceutical twin-screw wet granulation in view of detailed process understanding. Int. J. Pharm. 529, 678–693. https://doi.org/10.1016/j.ijpharm.2017.07.045

Vervaet, C., Remon, J.P., 2005. Continuous granulation in the pharmaceutical industry. Chem. Eng. Sci. 60, 3949–3957. https://doi.org/10.1016/J.CES.2005.02.028

Zou, H., Hastie, T., 2005. Regularization and variable selection via the elastic net. J. R. Stat. Soc. Ser. B (Statistical Methodol. 67, 301–320. https://doi.org/10.1111/J.1467-

905

910

915

Appendix A

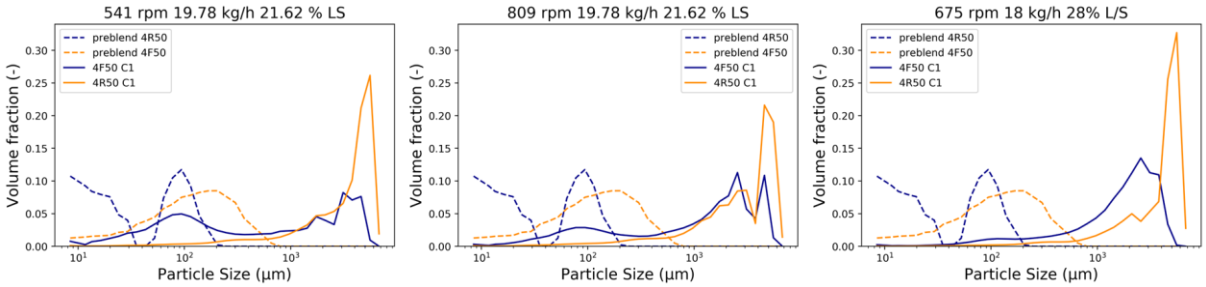

Fig. 11. Particle size distributions of the formulation preblend and granules produced during wetting for formulations 4R50 and 4F50.

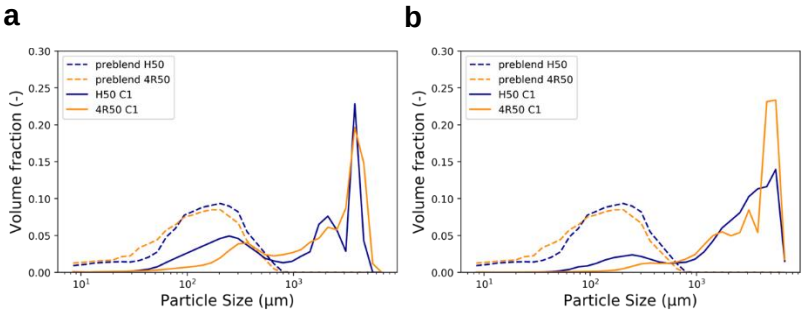

Fig. 12. Particle size distributions of the formulation preblend and granules produced during wetting for formulations H50 and 4R50. The lowest (a) and highest (b) L/S ratio for each formulation (Table 2) was used while MFR (20 kg/h) and S (675 rpm) were kept at center point level.

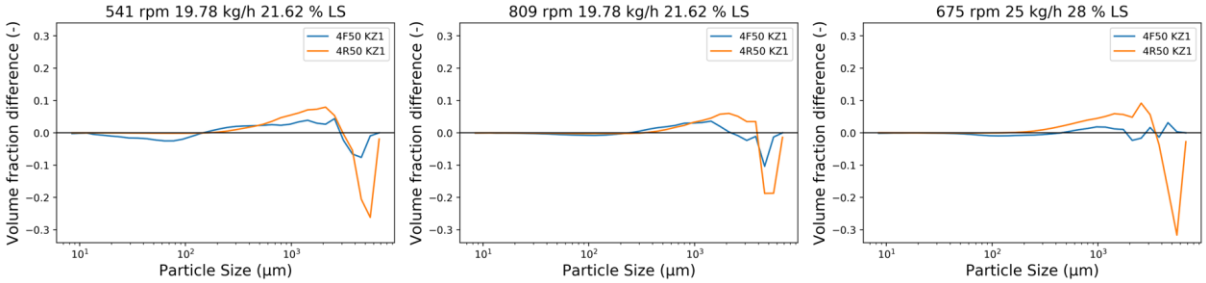

Fig. 13. Change in the particle size distributions in the first kneading compartment (KZ1) for formulations 4F50 and 4R50.

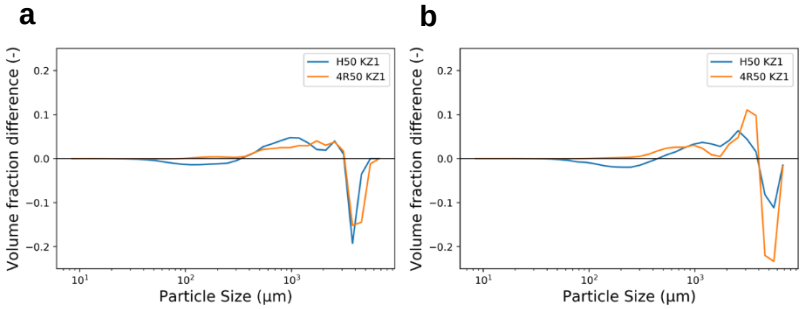

Fig. 14. Change in the particle size distributions in the first kneading zone (KZ1) for formulations H50 and 4R50. The lowest (a) and highest (b) L/S ratio for each formulation (Table 2) was used while MFR (20 kg/h) and S (675 rpm) were kept at center point level.

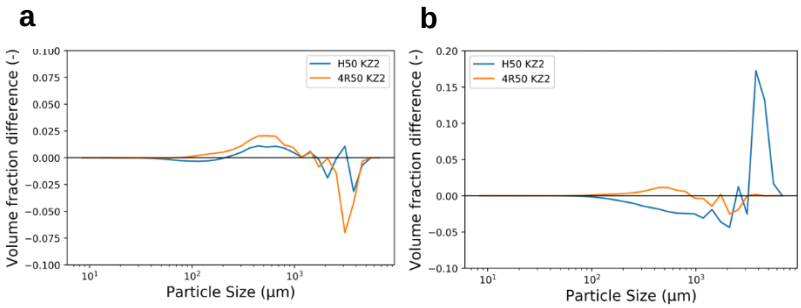

Fig. 15. Change in the particle size distributions in the second kneading zone (KZ2) for formulations H50 and 4R50. The lowest (a) and highest (b) L/S ratio for each formulation (Table 2) was used while MFR (20 kg/h) and S (675 rpm) were kept at center point level.

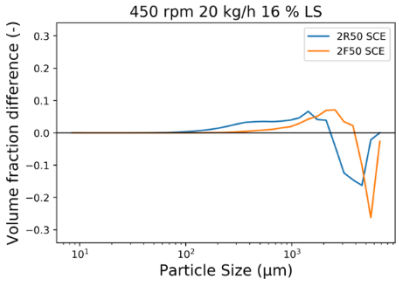

Fig. 16. Change in the particle size distributions in the size control elements (SCE) when applying identical TSG process settings for formulations 2R50 and 2F50.

Appendix B

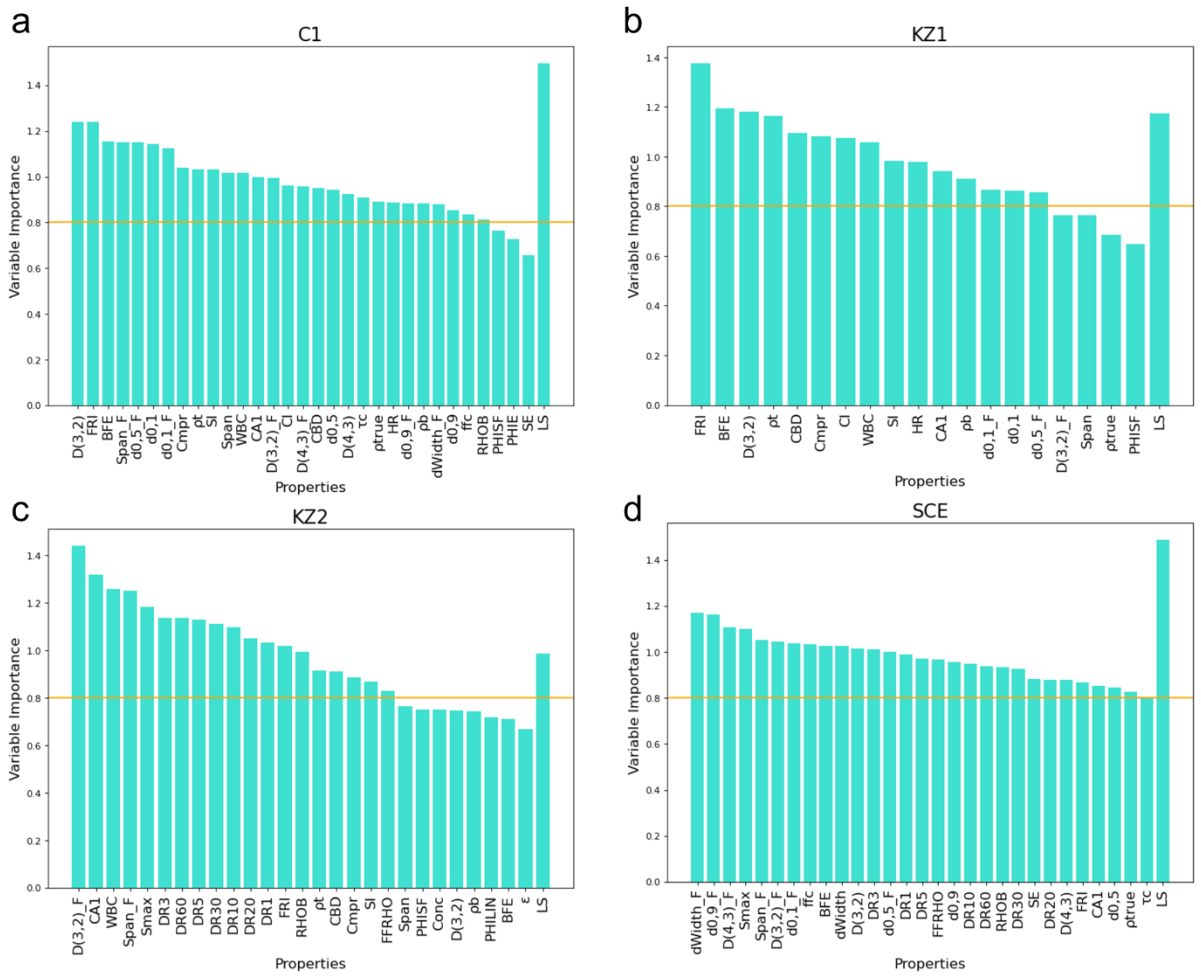

Fig. 17. VIP plots of PLS models for the change in granule size in (a) the wetting compartment (C1) (b) the first kneading zone (KZ1) (c) the second kneading zone (KZ2) (d) the size control elements (SCE).

PLS models for granule AR were developed after excluding outliers and non-relevant input variables (see Section 3.6.2). The number of variables and observations used for the model development became 29 variables and 102 observation (C1), 35 variables and 101 observations (C3), 29 variables and 101 observations (C5), and 30 variables and 91 observations (C6).

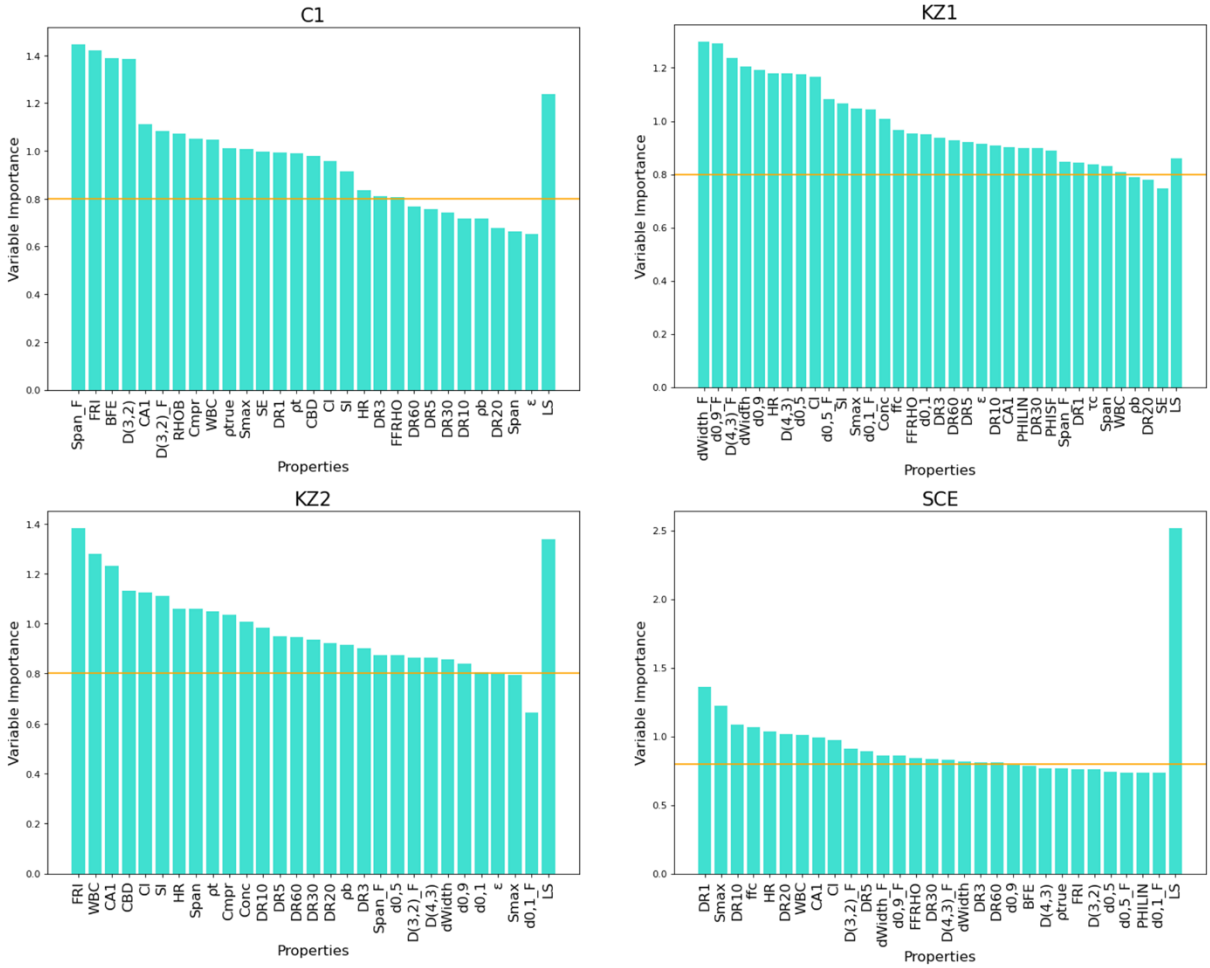

Fig. 18. VIP plots of PLS models for granule AR in the wetting compartment (C1) and the change in granule AR in the first kneading zone (KZ1) the second kneading zone (KZ2) and the size control elements compartment (SCE).

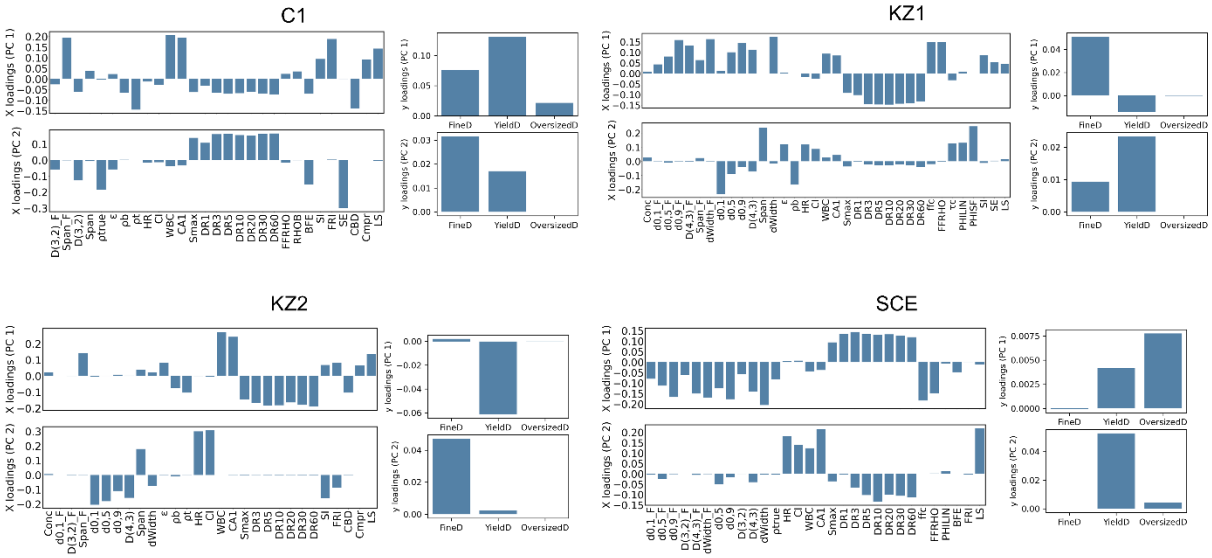

Fig. 19. Loading plots of PLS models for the granule AR in the wetting compartment (C1) and the change in granule AR in the first kneading zone (KZ1), the second kneading zone (KZ2) and the size control elements (SCE).

Appendix C

1. Material characterization methods

- Laser diffraction

Particle size distribution for powders and formulation blends was assessed using a Mastersizer® S (Malvern Instruments, Worcestershire, UK) through laser diffraction. Wet and dry dispersion methods were employed to determine a volume-based particle size distribution. For wet dispersion, Miglyol 812 (Fagron, Cappele aan den Ijssel, Netherlands) was used as a dispersant, with a stirrer speed set at 1500 rpm. Dry dispersion measurements involved feeding powder towards a 300 F lens at 3G, using a standard jet pressure of 2 bar. Each powder underwent triplicate measurements, analyzed with Mastersizer® S software. Key parameters included d10, d50, and d90 representing the 10%, 50%, and 90% cumulative under-size fractions. Additional metrics encompassed D[3,2] for surface-weighted mean and D[4,3] for volume-weighted mean. Particle size distribution characterization utilized dWidth (d90-d10) and span (dWidth/d50). A range of descriptors was gathered via laser diffraction to effectively capture particle size distribution information.

- Bulk and tapped density

Bulk (ρb) and tapped (ρt) density (g/mL) were determined in triplicate using a 250 mL graduated cylinder equipped with a tapping device (J. Engelsman, Ludwigshafen, Germany). 50g of powder (denoted as m) was gently added to the cylinder, and initial (Vb) and post-tapping (Vt) volumes (mL) were recorded. Bulk and tapped densities as well as the Hausner Ratio (HR) and Compressibility Index (CI) were calculated using Equations [1] to [4].

$$\rho b = \frac{m}{V_b} \quad [1]$$

$$\rho t = \frac{m}{V_t} \quad [2]$$

$$HR = \frac{V_b}{V_t} \quad [3]$$

$$CI = \frac{V_b - V_t}{V_b} \quad [4]$$

- True density and porosity

The true density ([ρtrue] = g/mL) for all materials was determined using an AccuPyc 1330 helium pycnometer (Micromeritics, Norcross, GA, USA) with an equilibration rate of 0.0050 psig/min and 10 purges. Each powder underwent triplicate measurements. Powder bed porosity (ε) was computed using Equation [5].

$$\varepsilon = 1 - \frac{\rho_b}{\rho_{true}} \quad [5]$$

- Water binding capacity.

Water binding capacity ([WBC] = %) reflects a powder's water-holding ability. Each 5.00 g of powder (mdry) was placed into centrifuge tubes. Next, 20 mL of demineralized water was added, and the tubes underwent centrifugation (Heraeus Multifuge 3 S-R, Thermo Scientific, USA) at 4000 rpm for 25 min. After removing the supernatant, the sample weight ([mwet] = g) was noted. WBC was calculated using Equation [6]. Negative values resulting from powder dissolution during measurement were treated as zero.

$$WBC = \left(\frac{m_{wet} - m_{dry}}{m_{dry}}\right) \times 100 \quad [6]$$

- Contact angle

Wettability was assessed through contact angle measurements using a drop shape analyzer (DSA30, Krüss, Hamburg, Germany). This analysis employs image analysis to determine contact angles from images and surface tensions. The sessile drop method was employed, where double-sided adhesive tape affixed to a glass plate was saturated with powder. These samples were prepared in triplicate, and 3 separate 5 µL water droplets (NE44 needles Ø 0.5 mm, Krüss, Germany) were placed on them. Contact angles ([CA] = °) were measured at 1 (CA1), 30 (CA30), and 60 (CA60) seconds after droplet release using the Young-Laplace method (Equation [7]):

$$\Delta p = \sigma\left(\frac{1}{r_1} + \frac{1}{r_2}\right) \quad [7]$$

Here, Δp (Pa) represents the pressure difference across the fluid interface, σ (in J/m2) denotes surface tension, and r_1 and r_2 (m) signify the radii of curvature. The obtained surface tension was used for calculating the contact angle by the analyzer.

- Solubility

To determine maximal solubility ([S_{max}] = g/100 mL), excess powder was added to 200 mL of demineralized water, creating a saturated solution with undissolved powder. Maintaining a constant temperature of 23°C, a stirring bar ensured proper wetting. Light and evaporation were prevented using Parafilm and aluminum foil. After 12 hours of stirring and 12 hours of rest, the supernatant was filtered with a cellulose-based filter (Grade 2, Whatman, USA). Filtrate analysis was conducted via UV-VIS spectrophotometry (UV-1650 PC, Shimadzu, Suzhou New District, China). A calibration model determined S_{max} for each powder, with known values for microcrystalline cellulose and hydroxypropylmethylcellulose (1x10-5 g/100 mL) due to their insolubility and water-swelling properties.

- Loss on drying

Residual moisture content of the powders was determined in triplicate using a Mettler Toledo HC103 Halogen Moisture Analyzer (Mettler-Toledo, Zaventem, Belgium). A 5 g sample was dried at 105 °C until moisture content change was less than 0.1% within 30 seconds, and the % loss on drying (LoD) was recorded.

- Angle of repose

Powder flow properties were assessed using the GranuHeap™ (Granutools, Awans, Belgium), which determined the angle of repose (AoR) and static cohesive index (SCI). AoR represents the angle of an isosceles triangle with the same surface as the projected powder heap. SCI quantifies the deviation of the heap from an ideal conical shape. Cohesive powders typically exhibit a larger AoR and higher SCI.

The process involved pouring 60 mL of powder onto a cylindrical support via an initialization tube. The tube was lifted at a constant speed of 5 mm/s, forming a powder heap on the support. The support was then rotated at 1 rpm, capturing 16 images, each 11.25° apart. Granutools' custom heap recognition algorithm performed image analysis.

- Dissolution rate

To determine dissolution rates, a closed USP4 Flow-Through Dissolution System (Sotax, Allschwil, Switzerland) was utilized, consisting of:

1. A piston pump (Sotax Cp 7–35) to transport demineralized water at 25.0 mL/min (pump speed: 110 rpm).

2. Two flow cells (Sotax CE 7 smart) containing a membrane (Float-A-Lyzer G2 Dialysis Device, Spectrum Laboratories) with a 1 mL volume and a 1000kD molecular cut-off value. Each membrane held 200 mg of powder.

3. Two media reservoirs with 250 mL of dissolution medium.

4. An autosampler (Agilent 8000 Dissolution Sampling Station) linked to the media reservoirs to collect 5 mL samples at 1, 3, 5, 10, 20, 30, and 60 minutes.

Collected samples were analyzed by UV–VIS spectrophotometry (UV-1650 PC, Shimadzu, Suzhou New District, China). A calibration model was established to determine concentration for each powder, except for microcrystalline cellulose, lactose, and hydroxypropylmethylcellulose. Microcrystalline cellulose wasn't measured due to insolubility, while hydroxypropylmethylcellulose was omitted due to swelling concerns. Lactose, which doesn't absorb UV, was indirectly measured using an enzymatic detection kit (Enzym Bio-analysis Lactose/D-glucose, R-biopharm AG, Darmstadt, Germany). This kit measured concentrations by detecting nicotinamide-adenine dinucleotide hydrogenate after enzymatic reactions. The fraction of powder dissolved after specific time intervals (DR1, DR3, DR5, DR10, DR20, DR30, and DR60) was calculated for all measured powders.

- Specific surface area.

The samples underwent a 24-hour degassing process at 60°C in a vacuum using VacPrep (Micrometrics, Norcross, USA). They were subsequently purged with nitrogen for 1 hour to eliminate impurities. Nitrogen adsorption measurements were then conducted using TriStar II (Micrometrics, Norcross, USA), and the specific surface area (SSA) was determined from the adsorption isotherm using the Brunauer–Emmett–Teller theory.

- Ring shear test.

Powder flowability and cohesivity were assessed in triplicate using a ring shear tester (RST-XS, Dietmar Schulze Schüttgutmesstechnik, Wolfenbüttel, Germany). The shear stress (τ) was plotted against the applied normal stress (σ) to construct the yield locus and Mohr stress. From these, the unconfined yield stress ([σ_c] = Pa) and major principal stress ([σ_1] = Pa) were determined to compute the dimensionless flow function coefficient (ffc) as a measure of flowability (Equation [8]).

$$ffc = \frac{\sigma_1}{\sigma_c} \quad [8]$$

Additionally, the consolidated density-weighed flow (ff_{rho}) (Equation [9]) was calculated to characterize flow under the influence of gravity. Here, ρ_w denotes the density of water (i.e., 1 g/mL) and $\rho_{consol}$is the density under consolidation (1000 Pa).

$$ff_{rho} = ffc \times \frac{\rho_{consol}}{\rho_w} \quad [9]$$

Other derived parameters included:

the linear angle of internal friction (φ_{lin}): the slope of the yield locus

the effective angle of internal friction (φ_e): the angle of the straight line through the origin of the σ,τ-diagram and tangent to the greater Mohr circle

the angle of internal friction at steady-state flow (φ_{sf}): the slope of the straight line through the origin of the σ,τ-diagram and the pre-shear data point

the powder cohesion (τc): the shear stress needed to initiate powder flow when no normal stress is applied (i.e., σ = 0).

- Powder rheology.

A FT4 powder rheometer (Freeman Technology, Tewkesbury, UK) was utilized to evaluate multiple powder flow properties, with stability, variable flow rate, and compressibility tests conducted in triplicate. Each test involved a pre-conditioning phase to ensure uniform packing of powder particles. For the stability and variable flow rate tests, the powder was placed into the 50 mm x 160 mL and 50 mm x 85 mL split vessels, respectively, and conditioned using a 48 mm blade.

Stability and Variable Flow Rate:

Initially, the Conditioned Bulk Density (CBD) of the powder was determined. Subsequently, the flow energy (E) in millijoules (mJ) was measured by moving a rotating blade up and down through the powder bed. Seven test cycles with identical conditions were performed to obtain a stable flow energy. The blade tip speed was set at 100 mm/s, and the flow energy (E) was calculated from the work required to move the blade through the powder from the top to the bottom of the vessel. Following this, the flow energy was measured while gradually reducing the blade tip speed (100, 70, 40, and 10 mm/s) in tests 8 to 11. The resulting parameters included the Basic Flow Energy (BFE) (flow energy at the 7th test in mJ), Stability Index (SI)

(calculated with Equation [10]), Flow Rate Index (FRI) (calculated with Equation [11]), and specific energy SE (in mJ/g) (calculated with Equation [12]).

$$SI = \frac{E\_test\ 7}{E\_test\ 1} \quad [10]$$

$$FRI = \frac{E\_test\ 11}{E\_test\ 8} \quad [11]$$

$$SE\ (\frac{mJ}{g}) = \frac{(up\ energy\ cycle\ 6 + up\ energy\ cycle\ 7)/2}{sample\ mass\ (g)} \quad [12]$$

Compressibility:

To assess compressibility, the powder was subjected to increasing normal stress levels (σ) ranging from 0.5 to 15 kPa, utilizing a vented piston. Compressibility ([Cmpr] = %) was defined as the relative change in volume at 15 kPa.